Materials and Structures (2026) 59:388
https://doi.org/10.1617/s11527-026-03258-3

ORIGINAL ARTICLE

From fabrication process to structural performance: exploring test procedures and design models for digitally fabricated concrete

Sven Engel · Eduarda Dilkin · Martin Classen

Received: 19 May 2026 / Revised: 17 August 2026 / Accepted: 20 August 2026
© The Author(s) 2026

Abstract Digital fabrication enables new possibilities for structurally optimized and resource-efficient reinforced concrete construction. In particular, extrusion-based 3D concrete printing (3DCP) allows the production of load-adapted geometries without conventional formwork. However, the structural application of reinforced 3D-printed concrete remains limited due to unresolved challenges regarding reinforcement integration and the applicability of existing structural design approaches. This paper presents a multimodal fabrication strategy combining 3DCP, casting, and integrated carbon-fiber reinforced polymer (CFRP) reinforcement for the digital production of reinforced concrete members. To investigate the resulting structural behavior, a comprehensive experimental program was conducted covering material characterization, bond behavior, bending, shear, and punching shear. Particular focus was placed on the interaction between fabrication-induced characteristics and structural load-transfer mechanisms. The experimental investigations demonstrate that optimized nozzle orientation significantly improves the bond behavior between CFRP reinforcement and 3D-printed concrete. Compared to cast reference specimens, the bond capacity of the printed specimens was reduced by 23–41%, depending on the nozzle orientation. Structural tests on beams revealed that conventional sectional analysis approaches can successfully predict flexural behavior. In contrast, the experimentally observed shear resistance of the beam without shear reinforcement was approximately 48% lower than the guideline-based prediction, highlighting the necessity of considering fabrication-induced anisotropy and interlayer delamination. The observed discrepancies are attributed to the anisotropic material behavior and reduced interlayer bond resulting from the layer-wise fabrication process. To address these effects, an existing physics-based shear model was critically evaluated and extended for application to digitally fabricated concrete members. In particular, the Shear Crack Propagation Theory (SCPT) was extended by incorporating interface delamination mechanisms specific to 3D-printed concrete. In combination with experimentally derived reinforcement contributions, the proposed hybrid modeling approach reproduced the experimentally observed shear capacities with deviations below 9%. The proposed framework demonstrates that reliable structural design of reinforced 3D-printed concrete cannot rely solely on conventional empirical approaches but requires mechanics-based models explicitly accounting for fabrication-induced characteristics. The presented methodology provides a transferable framework linking digital fabrication processes with

S. Engel (✉) · E. Dilkin · M. Classen
Chair and Institute of Structural Concrete, RWTH Aachen University, Aachen, Germany
e-mail: sengel@imb.rwth-aachen.de

S. Engel · M. Classen
Cluster of Excellence CARE, TU Dresden and RWTH Aachen University, Dresden, Germany

Published online: 16 September 2026

structural performance and establishes a basis for the development of future design provisions for reinforced 3D-printed concrete.

Keywords Structural performance of 3D-concrete printing: bond, bending, shear, punching · Reinforcement strategy · Non-metallic reinforcement · Modeling

1 Introduction

The construction sector is resource-intensive and a major source of global CO_2 emissions, largely due to the excessive use of cement-based materials [1–3]. Although load path optimized designs offer the potential to improve material efficiency, conventional formwork limits their realization, making digital fabrication a promising alternative [4–9]. Extrusion-based 3D concrete printing (3DCP) enables the formwork-free production of complex geometries by translating digital models into layer-wise deposition paths, making it particularly well suited for load-adapted ribbed structures that enable efficient load transfer through load-adapted geometries [10, 11]. Despite these advantages, the structural application of 3DCP remains limited. In particular, the absence of standardized testing methodologies, processing procedures, and approval frameworks continues to hinder the widespread implementation of 3D printing in concrete construction [12]. Furthermore, effective reinforcement strategies that ensure structural performance and compliance with engineering standards are still lacking [13, 14]. Digitally fabricated concrete differs fundamentally from conventional reinforced concrete due to its anisotropic material behavior [15], which arises from the layer interfaces [16] as well as non-standard reinforcement configurations [5]. As a result, the adequacy of existing design models in capturing key mechanisms such as bond [17], shear transfer [18–21], and bending resistance needs to be critically evaluated. This paper investigates a reinforcement concept for 3DCP and analyzes the load-bearing behavior of digitally fabricated structures. The approach links fabrication-induced characteristics with structural performance and is demonstrated on ribbed components as a representative class of load-adapted structures [14, 22, 23], while assessing the applicability of existing design models for predicting the behavior of such members.

2 Reinforcement concepts for 3DCP

The integration of reinforcement is essential for structural applications of 3DCP due to the limited tensile capacity and brittle behavior of unreinforced concrete. Despite numerous proposed approaches, no solution has yet achieved a satisfactory balance between structural performance, automation and process compatibility. In the following, a short overview of the integration of longitudinal and shear reinforcement is given. A comprehensive review is provided in [14].

2.1 Longitudinal reinforcement

Longitudinal reinforcement concepts in 3DCP primarily aim to enhance load-bearing capacity under bending by aligning reinforcement elements with principal stress directions. Existing approaches include the use of fiber-reinforced mixtures [24, 25] and the integration of continuous elements such as cables [26–29] or rebars [30] during printing. While these concepts demonstrate the feasibility of integrating longitudinal reinforcement into extrusion-based 3DCP, they are generally limited to reinforcement aligned with the printing direction. Consequently, they mainly improve flexural resistance but provide little contribution to interlayer load transfer or shear resistance. In addition, several concepts require dedicated end-effectors or process interruptions, limiting their applicability for automated large-scale production.

2.2 Shear reinforcement

In contrast to longitudinal reinforcement, the integration of shear reinforcement in 3DCP is considerably more challenging, as it requires reinforcement elements that intersect printed layers and must enable load transfer across interfaces. Such reinforcement is essential to prevent brittle shear failure and ensure structural integrity of load-bearing components. Existing concepts demonstrate the feasibility of integrating shear reinforcement before [31], during

[32–35], or after [36] the 3DCP process. However, many approaches require manual intervention, dedicated fabrication equipment, or additional joining processes, reducing the degree of automation and process robustness. Furthermore, only limited knowledge is available regarding the resulting bond mechanisms between reinforcement and layered concrete as well as their influence on structural shear behavior [37].

3 Design models

The structural design of reinforced concrete relies on well-established models to estimate resistance associated with key mechanisms such as bond, shear, and bending. Several of these formulations are empirically derived and have therefore been calibrated by using a comprehensive experimental database for conventionally cast concrete and standardized reinforcement layouts, relying on assumptions of homogeneous material behavior and well-defined interaction between concrete and reinforcement.

In the context of digital fabrication, however, these assumptions are no longer fully valid and require further investigations. The structural response of 3D-printed concrete members is strongly influenced by printing-induced anisotropy, where the mechanical properties and failure behavior depend on the loading direction relative to the deposited filaments and interlayer interfaces. In addition, reinforcement is often integrated in non-standard configurations aligned with the fabrication process, resulting in structural behaviors that differ from those of conventionally cast reinforced concrete.

To capture these complexities, various numerical modeling strategies have been proposed, ranging from macro-scale continuum approaches to interface-based formulations that explicitly represent interlayer boundaries, as well as meso-scale discrete models capable of describing localized cracking and filament interaction. A comprehensive overview of numerical modeling approaches is given in [38].

At the structural level, recent studies have demonstrated that conventional reinforced concrete design approaches for shear cannot be directly transferred to 3D-printed members without modification. A representative example is provided [39, 40], where a large-scale reinforced 3D-printed beam was experimentally investigated. In this case, comparison of the test results with Eurocode-based design equations [41] led to good agreement for the prediction of the flexural resistance, whereas the predicted shear capacity overestimated the experimental value by approximately 51%. This highlights the pronounced sensitivity of shear behavior to interlayer interfaces, anisotropy and reinforcement arrangement. Consequently, current research has to focus on adapting existing design approaches to account for governing parameters specific to additive manufacturing, such as filament orientation, interlayer bond quality and anisotropic load transfer mechanisms. While still representing a simplified approach, [42] proposed a modified shear design equation, incorporating an empirically derived reduction factor dependent on the shear span-to-depth ratio in order to better capture the experimentally observed shear behavior of 3DCP members. Although this represents an important step towards improved shear design, empirically calibrated reduction factors remain unable to capture the full variability inherent to 3DCP processes.

Consequently, a mechanics-based design framework that explicitly accounts for diverse fabrication-induced characteristics while simultaneously minimizing the dependence on extensive experimental calibration is still lacking. The following sections therefore first present the fabrication and experimental investigation of 3DCP structural members carried out in this study. Based on the observed structural behavior and failure mechanisms, a new approach for modeling the shear resistance of 3DCP members is subsequently introduced.

4 Description of the experimental campaign

4.1 Multimodal fabrication process

As already discussed, to fully exploit the potential of digital fabrication for reinforced concrete structures, new fabrication approaches are required that enable the controlled integration of reinforcement within layer-wise production processes. For this purpose, a multimodal, robot-assisted fabrication process is employed for the production of ribbed reinforced concrete members. The process combines 3DCP with concrete casting by integrating prefabricated CFRP

reinforcement elements, thereby exploiting the advantages of both fabrication methods. While casting enables the efficient production of planar elements using formwork, 3D printing allows for the formwork-free fabrication of complex geometries. Figure 1 illustrates the process on small-scale T-beams, which serve as representative ribbed structures. The fabrication process consists of several coordinated steps. First, a formwork for the base element is produced using 3D printing, which includes the printing of support structures for subsequent reinforcement placement (Fig. 1). This allows for the generation of customized geometries for formwork without additional tooling. In a second step, prefabricated CFRP reinforcement elements are positioned within the printed supporting structure. These L-shaped elements (Fig. 3) create a connection between the cast base element and the ribbed structure, ensuring adequate interaction between both components while also acting as shear reinforcement. Following reinforcement placement, the base element is produced by casting concrete into the printed formwork. Afterwards, the ribbed structure is printed directly onto the freshly cast element. The printing path is adapted to the reinforcement geometry, and the nozzle is guided along the reinforcement. The longitudinal reinforcement can be incorporated either (i) prior to printing by fixing thin CFRP strands to the shear reinforcement in the desired position, or (ii) during the printing process by briefly pausing the printing process and embedding the reinforcement into the freshly printed concrete. The latter approach is particularly suitable for larger CFRP rebars, which may otherwise interfere with nozzle guidance if fixed to the shear reinforcement.

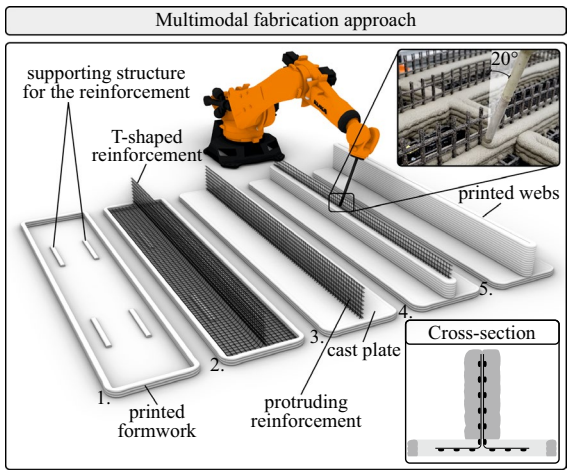


Fig. 1 Digital multimodal manufacturing process of ribbed CFRP-reinforced concrete members: 1. Printing the formwork of the plate and supporting structure for the reinforcement; 2. Integrating the reinforcement; 3. Grouting the plate; 4. Printing the ribs along the protruding reinforcement; 5. Finished ribbed component

Figure 1 illustrates the process on small-scale T-beams, which serve as representative ribbed structures for demonstrating the fundamental fabrication methodology. While the presented multimodal approach is transferable to a wide range of digitally fabricated reinforced concrete members, it was specifically developed for the automated prefabrication of ribbed reinforced concrete modules, where the precise coordination of multiple fabrication steps can be ensured under controlled production conditions [9, 43]. Furthermore, the concept is not limited to CFRP reinforcement, but can also be adapted to other reinforcement materials, such as steel, which can be integrated using automated welding-based fabrication processes [33].

4.2 Developed testing methodology and overview of the experimental program

Based on the presented fabrication approach, a comprehensive experimental program was developed to investigate the structural behavior of multimodally fabricated CFRP-reinforced concrete members (Fig. 2). The testing methodology follows a hierarchical approach, progressing from material characterization and local interaction mechanisms to structural member behavior and finally to the investigation of complex load-transfer regions in large-scale components. All specimens were manufactured based on the multimodal fabrication approach described in Sect. 4.1 and in [14].

For the proposed shear reinforcement concept, three reinforcement-related regions were identified as potentially critical for the structural behavior: (i) the straight CFRP reinforcement, (ii) the bond between the straight CFRP reinforcement and the surrounding 3D-printed concrete, and (iii) the preformed CFRP deflection region. Consequently, the experimental program was designed to investigate each of these mechanisms individually before evaluating their interaction at the structural member level.

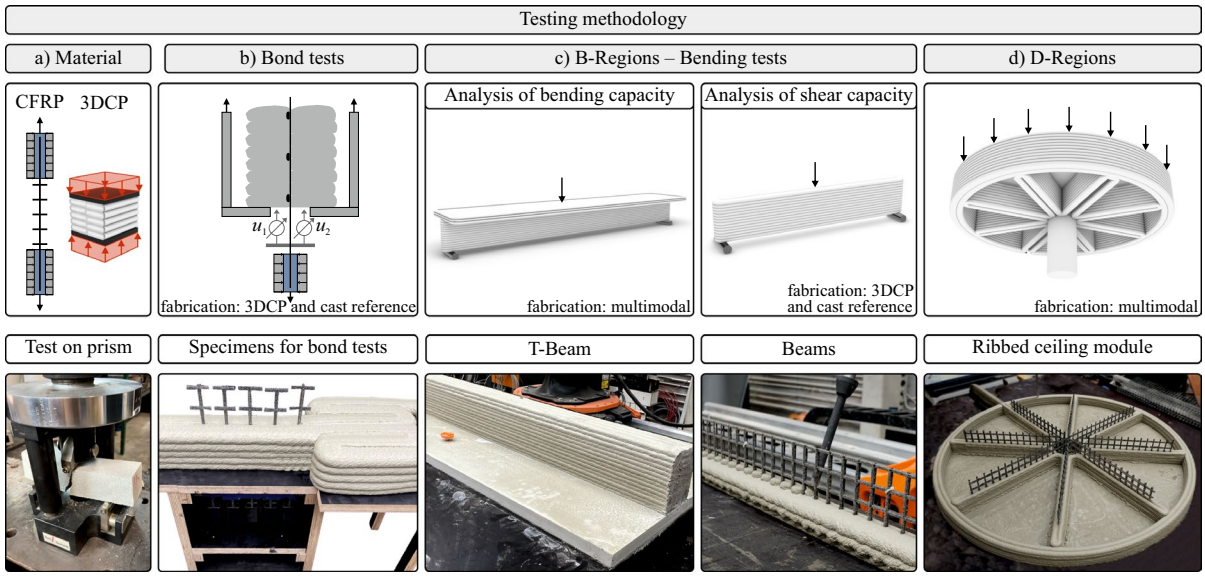


Fig. 2 Overview of the experimental program

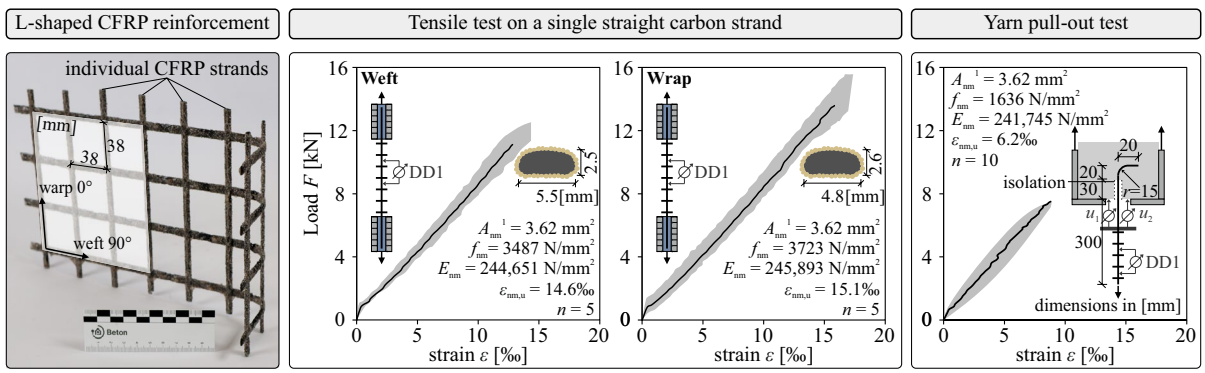


Fig. 3 Mechanical properties of the CFRP grid *Q95* (*solidian*)

Depending on the objective of the experimental investigations, either purely 3D-printed or multimodally fabricated specimens were used (Fig. 2). While the former enabled isolated investigation of individual material and structural mechanisms, the latter were used to evaluate the structural interaction of the multimodal fabrication process and its applicability to structural-scale components. In a first step, the mechanical properties of the constituent materials were characterized. This included experimental investigations on the anisotropic mechanical behavior of 3DCP as well as the tensile behavior of CFRP reinforcement, considering both straight and preformed reinforcement configurations (Fig. 2 a). In a second step, the local interaction behavior between reinforcement and concrete was investigated by means of pull-out tests based on [44] (Fig. 2b). These investigations focus exclusively on the bond and anchorage behavior of the straight CFRP reinforcement segments embedded in the printed concrete, representing the load-transfer mechanisms within the printed webs of the structural members.

Following the material and bond investigations, the structural behavior of B-regions was analyzed

experimentally. For this purpose, flexural behavior was investigated on a CFRP-reinforced T-beam subjected to three-point bending (Fig. 2c), while shear behavior was examined using 3D-printed beams tested under three-point bending (Fig. 2c). These investigations focused on crack formation and propagation, load transfer mechanisms, bending resistance, and shear capacity. Finally, the transferability of the developed reinforcement and design concepts to structural-scale D-regions was investigated using a load-adapted ribbed ceiling module subjected to punching shear loading (Fig. 2d). The large-scale ceiling module was used to evaluate the structural behavior of the multimodal fabrication approach and to assess its applicability to structural components.

5 Material

5.1 CFRP reinforcement

In this study, CFRP reinforcement, both in form of grids and rebars, is used. The proposed manufacturing approach benefits from CFRP due to its high tensile strength, minimal required concrete cover and slender profile [45, 46]. These properties make CFRP particularly suitable for integration into 3DCP [37]. As discussed in Sect. 2, the integration of shear reinforcement into 3DCP requires reinforcement concepts that are compatible with the layer-wise fabrication process. Unlike conventional reinforced concrete, where shear reinforcement is typically provided by closed steel stirrups with well-established mechanical anchorage, reinforcement concepts for 3DCP generally require open reinforcement configurations. In this study, preformed CFRP L-profiles are employed as shear reinforcement, resulting in fundamentally different anchorage and load-transfer mechanisms that require dedicated experimental investigation (Fig. 3). The integration of such profiles into 3D-printed structures results in reinforcement configurations consisting of both straight and geometrically deflected regions (Fig. 1). Consequently, different mechanical conditions arise along the reinforcement [14]. The load transfer in the straight segments is governed by its bond interaction with the surrounding printed concrete, while the deflected regions exhibit altered tensile behavior due to geometric effects. Therefore, the mechanical properties of both straight and deflected CFRP grid reinforcements are analyzed in the following sections. For the presented investigations, an epoxy-impregnated biaxial CFRP grid from the manufacturer *solidian*, labeled ANTICRACK FORM Q95-CCE-38 and featuring a sand-coated surface, was used. The textile is characterized by a regular grid structure with a yarn spacing of 38 mm and a nominal filament cross-sectional area of 3.62 mm^2 (without epoxy impregnation) [47].

5.1.1 Behavior of straight CFRP strands

To characterize the mechanical behavior of the reinforcement, tensile tests were conducted on individual straight CFRP strands in accordance with [44] using a test speed of 1 mm/min. Since the investigated CFRP grid exhibits a biaxial structure, specimens were tested in both principal directions (warp and weft, see Fig. 3 (left)). These tests provide the reference tensile strength and stiffness of the material. In all cases, failure of the CFRP strands occurred within the free length. The results are presented in Fig. 3, showing the load-strain behavior of the CFRP grid in both directions. The mean ultimate tensile strength, obtained from five tests, is $f_{nm} = 3487$ N/mm^2 with a fracture elongation $\varepsilon_{nm,u} = 14.6‰$ in weft direction and $f_{nm} = 3723$ N/mm^2 ($\varepsilon_{nm,u} = 15.1‰$) in warp direction.

5.1.2 Behavior of preformed CFRP strands

In addition, the mechanical performance of the preformed CFRP reinforcement was investigated. The preforming process introduces geometric deflections, which are required to improve anchorage within the structural system. However, these deflections influence the tensile properties of the material [48]. In curved regions, fiber alignment is altered and local stress concentrations occur, leading to a reduction in effective tensile strength and stiffness compared to straight strands, which must be considered in structural design. To quantify this effect, modified yarn pull-out (YPO) tests, based on [48], were conducted on deflected reinforcement strands.

The specimens were defined by a tail length of 20 mm, a free length of 300 mm, an isolation length of 30 mm, and an anchorage depth of 20 mm (Fig. 3). The isolation in the test block was achieved by placing plastic tubes (Ø5 mm) over the reinforcement,

which was then sealed with heat-shrink tubing. After fabrication, the specimens were covered with foil and tested after 21 days. The tests were conducted under deformation control with a crosshead speed of 0.2 mm/min. The upper connection allowed full rotational freedom, ensuring axial loading of the yarn. For specimens with sufficient free length, the modulus of elasticity was determined using a strain sensor (DD1) attached directly to the yarn (Fig. 3). Additionally, two laser sensors measured the elongation between the steel fixture and a measurement clip fixed to the yarn, allowing the measurement of the slip at the loaded end. In all specimens the rupture occurred in the deflection of the CFRP strand. The results demonstrate a reduction in tensile strength of approximately 55% compared to the straight strands.

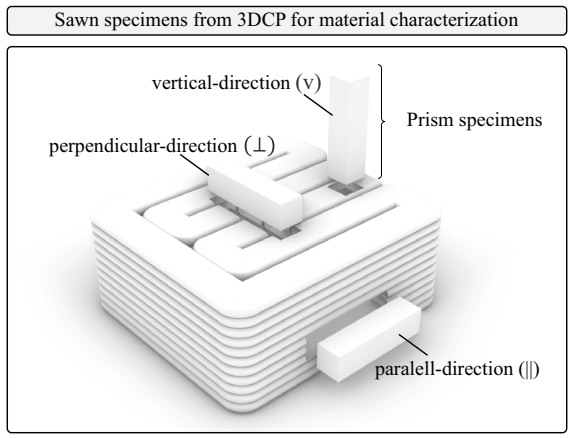


Fig. 4 Demonstration of the anisotropic behavior of 3D-printed concrete—orientation of the specimens used for material characterization

5.2 3D-printed concrete

In this study, the printable mortar *Weber 3D 160-1* from the manufacturer *Saint-Gobain* was used. The mixture is based on Portland cement (CEM I) and incorporates limestone aggregates with a maximum particle size of 1 mm, as well as fibers, chemical additives, and rheology modifiers. The formulation provides an open time of approximately 1h and has a water-to-cement ratio lower than 0.45 [49].

Due to the anisotropic material behavior of 3DCP, test specimens for material characterization were prepared and tested in different directions (Fig. 4). The mechanical properties of the material were determined on the day of testing for each test series and are presented individually in the following chapters. The compressive and flexural tensile strengths were determined in accordance with [50–52].

6 Bond behavior

6.1 Motivation

The proposed CFRP L-profiles consist of geometrically deflected segments and straight segments embedded within the printed webs. Whereas Sect. 5 investigated the mechanical behavior of the deflected regions, the structural behavior of the printed webs is governed by the bond between the straight CFRP segments and the surrounding 3D-printed concrete. In contrast to conventionally cast concrete, this bond is strongly influenced by the layer-wise fabrication process, which affects the local embedding conditions and the stress transfer at the reinforcement–concrete interface. Consequently, the achievable bond strength and anchorage behavior differ from those of conventional reinforced concrete. The following section therefore focuses on the experimental investigation of the bond behavior of the straight CFRP segments embedded within the printed concrete.

6.2 Experimental program

The bond behavior was investigated using single-sided pull-out tests (SPOc) for non-metallic reinforcement in accordance with [44, 53], adapted for application to 3DCP. The test setup consists of a printed concrete specimen embedding a single CFRP strand, which is subjected to displacement-controlled loading at a rate of 1 mm/min while the concrete specimen is held fixed (Fig. 6). The slip of the reinforcement was measured using two laser displacement sensors positioned at the loaded end of the reinforcement. The average slip was determined as: $u_m = (u_1 + u_2) / 2$.

The specimens were manufactured using the multimodal fabrication process described in Sect. 4.1. For each test series, individual longitudinal strands were cut from the original CFRP grid

(weft-direction; Fig. 3) while retaining the attached transverse strands (Fig. 5). During the bond tests, only the longitudinal strand was subjected to tensile loading, whereas the remaining transverse strands were intentionally preserved to maintain the original reinforcement geometry and representative local anchorage conditions. During printing, the concrete was deposited from both sides of the reinforcement in order to achieve sufficient embedding and symmetric confinement conditions (Fig. 5). Particular attention was given to the local material flow around the reinforcement, as the penetration and consolidation of fresh concrete within the CFRP grid significantly influence the bond conditions. Therefore, the material feed rate was adjusted to ensure sufficient mortar penetration through the reinforcement structure while maintaining the intended specimen geometry.

To investigate the influence of the printing process on bond behavior, different nozzle inclinations (0°, 10°, 20°, and 30°) relative to the reinforcement direction were examined (Fig. 6). The underlying hypothesis was that extrusion towards the reinforcement improves the local bond conditions by enhancing the interpenetration between adjacent concrete filaments and reducing interfacial discontinuities in the vicinity of the reinforcement. For each parameter configuration, five specimens were produced by printing a continuous beam-like element, which was subdivided into individual specimens after approximately one hour by inserting steel plates into the fresh concrete (Fig. 5). The cross-section consisted of two adjacent filaments with a total width of 80 mm and a depth of 38 mm, corresponding to the geometry of the employed CFRP grid. The specimen height was varied in order to investigate different embedment lengths. After fabrication, all specimens were moistened and covered with foil.

In addition to the pull-out specimens, the printing path included sections for material characterization (Fig. 5). Prism specimens were extracted to determine the mechanical properties of the printed concrete. Particular focus was placed on the flexural tensile strength perpendicular to the printing direction ($f_{ctm,3DCP-\perp}$), as this parameter characterizes the interfacial behavior between adjacent printed filaments and is therefore directly related to the bond conditions of the embedded reinforcement. Compressive and flexural strengths were determined in accordance

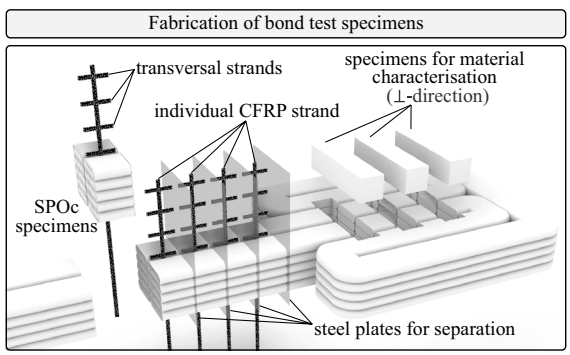


Fig. 5 Production of the SPOc-specimens

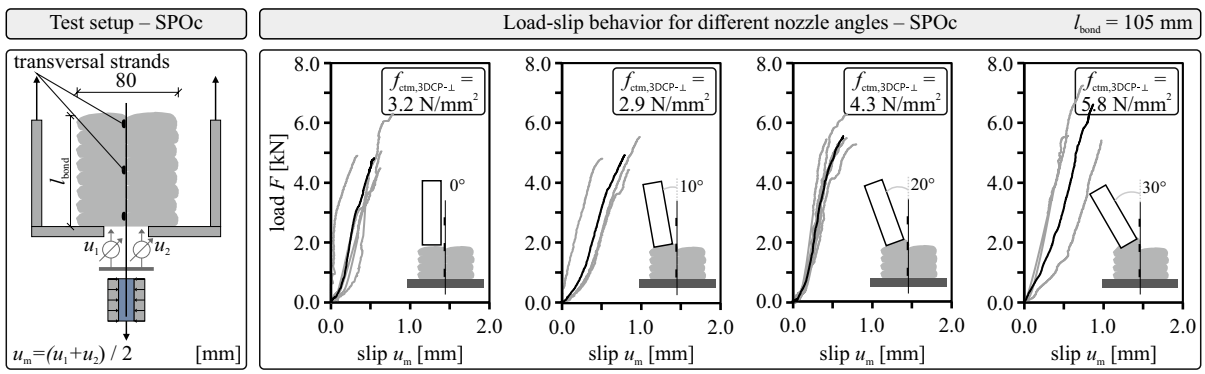


Fig. 6 Load–slip response obtained from single sided pull-out tests (SPOc)

Table 1 Overview of the bond test results

Codification	Fabrication	Nozzle angle [°]	l_{bond} [mm]	n [–]	a [–]	age [days]	$f_{cm,3DCP-\perp}$ [N/mm^2]	$f_{ctm,3DCP-\perp}$ [N/mm^2]	F_{max} [1] [kN]	VAR [kN]	ε_{max} [2] [‰]
Tests with straight CFRP strand	printed	20	45	4	1	18	44.0	–	4.4	0.5	5.0
	printed	20	75	3	1	18	48.0	4.6	4.7	0.3	5.3
	printed	20	105	5	1	19	49.7	4.3	5.6	0.4	6.3
	printed	20	105	3	2	18	45.1	6.7	11.2	1.5	6.3
	printed	0	105	4	1	19	48.9	3.2	4.4	0.8	5.0
	printed	10	105	3	1	19	42.4	2.9	4.9	0.6	5.5
	printed	30	105	3	1	19	41.5	5.8	5.7	0.5	6.4
	cast	-	105	4	1	13	58.3	8.4	7.5	0.6	8.5
Tests with deflected CFRP strand	printed	20	45	5	1	14	46.1	6.7	4.3	0.5	4.9
	printed	20	75	5	1	14	48.1	6.9	6.7	0.9	7.6
	printed	20	105	4	1	14	44.4	8.6	8.3	0.7	9.4

n: number of executed tests

a: number of CFRP strands

VAR: coefficient of variation for the SPOc results

[1]mean ultimate load

[2]strain per CFRP strand at ultimate load, determined based on E_{nm} = 244,651 N/mm^2 (Fig. 3)

with [52] and the corresponding results are presented in Fig. 6 and Table 1.

The following parameters were investigated systematically:

- Nozzle angle (0°, 10°, 20°, 30°),
- Manufacturing method (3D-printed, cast),
- Embedment length (45 mm, 75 mm, 105 mm),
- Number of CFRP strands (one or two strands).

6.3 Results and discussion

Figure 7 presents the load–slip response of specimens produced with different nozzle inclinations and a constant embedment length of l_{bond} = 105 mm. Initially, all specimens exhibit a reduced stiffness, which is attributed to the alignment and seating effects of the CFRP strands within the test setup at low load levels. With increasing load, the response becomes approximately linear, followed by a nonlinear regime prior to failure. All specimens failed due to splitting of

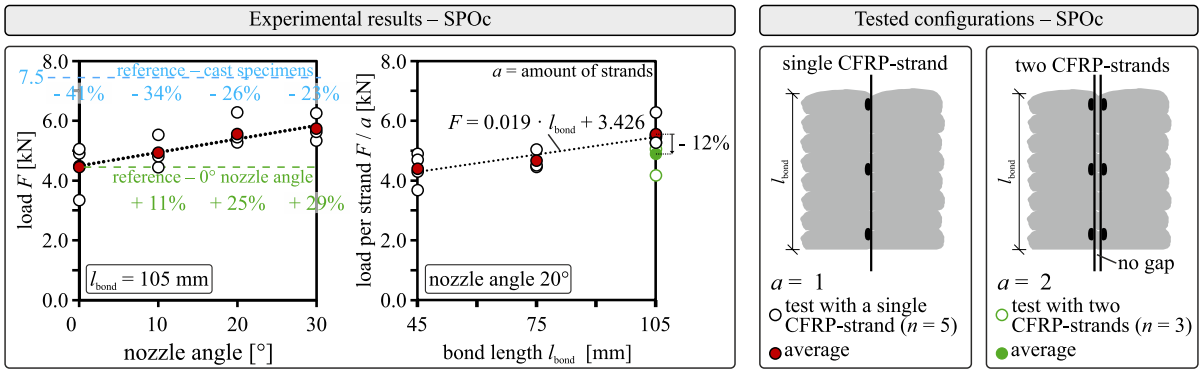


Fig. 7 Summary of the results of the SPOC tests: (left) load–nozzle angle relationship and load–bond length relationship; (right) comparison between the use of one and two CFRP strands

the surrounding concrete, with measured slip values below 1 mm at ultimate load.

The experimental results demonstrate a pronounced influence of the nozzle inclination on the bond performance. Increasing nozzle angles generally resulted in higher ultimate loads and improved bond behavior. This effect is attributed to enhanced material interpenetration and improved consolidation between adjacent concrete filaments. As a result, improved local interfacial properties and enhanced mechanical interaction between concrete and reinforcement are achieved. This interpretation is further supported by the experimentally determined flexural tensile strength perpendicular to the printing direction, which exhibits a similar trend (Fig. 6).

Among the investigated configurations, specimens produced with a nozzle inclination of 30° exhibited the highest bond capacity. Nevertheless, a nozzle angle of 20° was selected for the subsequent investigations, as it provides a favorable compromise between mechanical performance and process feasibility. Larger nozzle inclinations increase the complexity of the robotic fabrication process and may result in geometric conflicts between the nozzle and the reinforcement, particularly in densely arranged rib structures.

Reference tests were additionally conducted on cast concrete specimens with an embedment length of 105 mm using the same CFRP reinforcement type. To isolate the influence of the manufacturing process, the cast reference specimens were produced using the same printable mortar without modifying the material composition and were compacted on a vibrating table after casting. Compared to the cast reference specimens, the bond capacity of the printed specimens was reduced by approximately 23–41%, depending on the nozzle inclination (Fig. 7). This reduction highlights the influence of the layer-wise fabrication process on the bond conditions and demonstrates the sensitivity of the reinforcement–concrete interaction to the local deposition strategy.

In addition to the nozzle inclination, the influence of embedment length (45 mm, 75 mm, and 105 mm) was investigated (Fig. 7). The results indicate an approximately linear increase in ultimate load with increasing embedment length, demonstrating the governing influence of the available bond area on the load transfer capacity.

Furthermore, additional tests with two embedded CFRP strands were conducted in order to investigate the influence of an increased amount of shear reinforcement (Fig. 7). Compared to specimens with a single strand, the specimens containing two adjacent CFRP strands exhibited a reduction in bond capacity of approximately 12% relative to the bond area (l_{bond} = 105 mm) (Fig. 7). This reduction can be attributed to the limited concrete penetration and consolidation between the closely spaced reinforcement strands, resulting in reduced confinement conditions and impaired stress transfer at the reinforcement–concrete interface. Consequently, the effective bond area was reduced, leading to lower bond resistance.

6.4 Influence of hooks in bond performance

The following investigations evaluate a potential approach to improve the anchorage of the straight ends of the CFRP shear reinforcement embedded in the printed webs. Generally, the bond interaction between CFRP reinforcement and concrete is governed by the combined effects of adhesion, friction, and mechanical interlock. For straight CFRP strands, the load transfer is primarily controlled by adhesion and friction, while the contribution of mechanical interlock remains limited due to the relatively smooth reinforcement surface. Consequently, the straight end regions of the reinforcement represent critical locations with respect to anchorage performance, particularly in applications with limited available anchorage lengths such as shear reinforcement in thin-walled 3D-printed structures. This effect is further amplified in 3DCP due to the anisotropic material behavior of the printed concrete and the reduced interfacial properties between adjacent concrete filaments. In particular, the reduced flexural tensile strength of 3DCP perpendicular to the printing direction ($f_{ctm,3DCP-\perp}$) negatively affects the confinement and stress transfer mechanisms in the vicinity of the embedded reinforcement (Fig. 8). As a result, insufficient anchorage of straight CFRP strands may govern the structural performance and limit the effective activation of the reinforcement.

To improve the anchorage behavior of these straight reinforcement ends, geometrical modifications of the reinforcement were investigated by

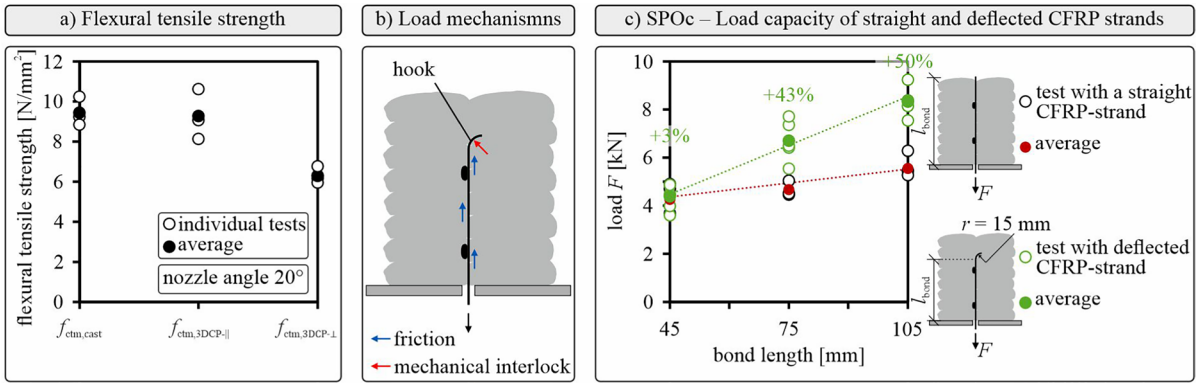


Fig. 8 Demonstration of the flexural strength of printed and cast concrete and the influence of improved anchorage using new shear reinforcement layout

introducing hook-shaped anchorage zones produced through thermoforming of the CFRP strands. In contrast to straight reinforcement ends, such hooks enable an additional form-fit load transfer mechanism by introducing a change in the force direction and thereby increasing the anchorage resistance. For the present investigations, hook-shaped CFRP ends were generated by thermoforming the reinforcement strands prior to printing. The resulting specimens were fabricated according to the multimodal process shown in Fig. 5 and investigated using single-sided pull-out (SPOc) tests with varying embedment lengths.

The experimental results demonstrate that thermoformed hooks significantly improve the anchorage performance of CFRP reinforcement embedded in 3DCP. Compared to straight reinforcement strands, substantially higher transferable loads were achieved, which indicates enhanced stress transfer and more effective activation of the reinforcement (Fig. 8). The increase in load-bearing capacity was found to be dependent on the embedment length, with improvements of up to 50% observed within the investigated parameter range. However, the integration of hook-shaped reinforcement ends introduces additional challenges for the printing process, as the modified reinforcement geometry interferes with the nozzle path and locally disturbs the material deposition process. Therefore, future developments should focus on adaptive manufacturing strategies in which the deformation of the reinforcement ends is integrated directly into the multimodal fabrication process.

7 Behavior under bending

7.1 Motivation

Particularly in slender and ribbed reinforced concrete members, the structural response under flexural loading is of extreme importance. Due to the multimodal fabrication approach, which combines casting and 3DCP, the load bearing behavior is influenced by the layer-wise deposition of the printed webs and the integration of reinforcement. For this reason, the bending behavior of a CFRP-reinforced, digitally fabricated concrete T-beam is experimentally investigated as a proof-of-concept to assess the applicability of established sectional analysis approaches to multimodally fabricated members.

7.2 Experimental program

7.2.1 Specimen and fabrication

To investigate the bending behavior of multimodally fabricated members, a three-point bending test was conducted on a T-beam specimen (Fig. 9). The specimen was manufactured following the multimodal fabrication approach, described in Sect. 4.1. The base plate, with a thickness of 40 mm, was cast in place, while the webs, with a width of 120 mm, were 3D-printed along the protruding reinforcement. The plate was produced using the same printable mortar. To obtain a castable consistency, the water content of the mortar was increased, and the concrete was compacted on a vibrating table after casting to ensure

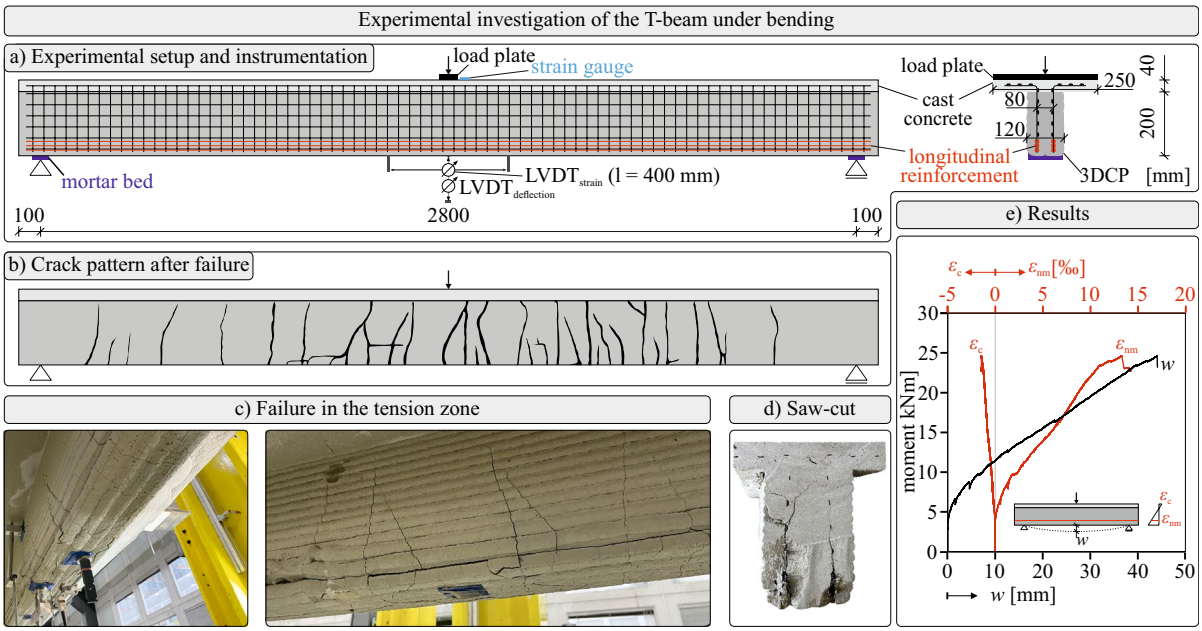


Fig. 9 Experimental investigation and structural response of the T-beam

proper consolidation. The printed webs were deposited directly onto the freshly cast base plate without additional surface preparation, thereby establishing the multimodal connection during fabrication. As shear reinforcement, two individual CFRP L-profiles (Fig. 9) were used and arranged with a spacing of approximately 80 mm, ensuring adequate bonding through embedding concrete from both sides (Fig. 9). The printing process was carried out at a speed of 100 mm/s, with a layer height of 15 mm and a filament width of approximately 30 mm. The print path was designed such that four filaments were deposited side by side: two filaments were printed between the CFRP profiles with a nozzle angle of 0°, while two additional filaments were applied outside the profiles using a nozzle angle of 20°. Longitudinal reinforcement was provided by twelve CFRP strands (Fig. 9). The average effective depth of the cross-section, d_m = 200 mm, was measured at the critical section after failure. The corresponding mechanical properties are summarized in Table 3.

The T-beam was cured under foil and tested after 44 days. The mechanical properties of the hardened cast and 3D-printed concrete are summarized

Table 2 Mechanical properties of the hardened concrete

Parameter		Manufacturing method	Specimen	Amount of tests	Mean
Flexural tensile strength	$f_{ctm,3DCP-\parallel}$	printed (∥-direction)	prisms (40×40×160 mm^3)	3	9.0 N/mm^2
	$f_{ctm,cast}$	cast		3	11.1 N/mm^2
Compressive strength	$f_{cm,3DCP-\parallel}$	printed (∥-direction)	prisms-halves	6	59.7 N/mm^2
	$f_{cm,cast}$	cast		6	69.2 N/mm^2
	$f_{cm,cyl}$	cast	cylinder (Ø150×200 mm^2)	3	62.0 N/mm^2
E-Modul	$E_{cm,3DCP-\parallel}$	printed (∥-direction)	prisms (40×40×160 mm^3)	5	24,881 N/mm^2
	$E_{cm,cast}$	cast	cylinder (Ø150×200 mm^2)	3	26,556 N/mm^2

in Table 2. For this study, both flexural and compressive strengths, as well as the Young's modulus, were determined for cast and 3DCP. Compressive and flexural tensile strength tests were conducted on prisms (40×40×160 mm^3) for both cast and 3DCP, with the printed specimens tested parallel to the printing direction, in accordance with [52, 54]. For each configuration, three specimens were tested. In addition, compressive strength tests were performed on cast cylinders (Ø150×200 mm^2) to provide reference values. For these tests, three specimens were evaluated in each case. The Young's modulus was determined on cast cylinders in accordance with [55] and on 3D printed prisms (40×40×160 mm^3) [52], with three tests conducted for each configuration.

7.2.2 Test-setup

To ensure uniform load transfer and to prevent torsional effects during the three-point bending test (Fig. 9), mortar beds were applied at the load introduction points to compensate for surface irregularities of the printed concrete (shown in purple in Fig. 9). The beams were supported on a pinned and a movable roller support. The vertical load was applied using a hydraulic actuator, with the applied force monitored by load cells integrated into the loading system. The test was conducted under displacement control at a midspan displacement rate of approximately 1 mm/min. During testing, vertical deflection was recorded, and strains in the compression and tension zones were measured using strain gauges and linear variable differential transformers (LVDTs). Furthermore, crack development was monitored using a photogrammetric measurement system based on digital image correlation (DIC). A stochastic speckle pattern was applied to one side of the beam, and measurements were carried out using the ARAMIS 2D DIC system from *Zeiss*.

7.3 Moment–deflection response and cracking behavior

The moment–deflection response of the specimen is shown in Fig. 9. Up to a moment of approximately M_I=6.5 kNm, the cross-section remained uncracked. Initial cracking occurred at this load level and at a moment of approximately 9 kNm the cracking pattern was fully developed. In the subsequent loading phase, the specimen exhibited an almost linear increase in deformation until failure. The maximum moment of 24.6 kNm was reached at a midspan deflection of 44 mm (Fig. 9), at which point failure occurred abruptly. At this stage, the measured strain in the tension zone, occurring in the longitudinal reinforcement, was approximately 13.2‰, while the compressive strain reached only −1.4‰ (Fig. 9). This indicates that the compressive capacity of the concrete was not fully utilized, likely due to the presence of the flange in the compression zone. Furthermore, no local cracking, slip, delamination, or failure was observed at the interface between the cast flange and the printed web throughout the test, indicating adequate composite action between both components. In contrast, the CFRP longitudinal reinforcement approached its tensile capacity, which is further supported by the local spalling of the surrounding concrete in the midspan region (Fig. 9). The crack patterns were documented throughout the test and after failure. The final crack pattern is shown in Fig. 9. The specimen exhibited a typical flexural cracking behavior, with predominantly vertical cracks in the midspan region. No critical crack patterns related to the layered printing process were observed. Only a few horizontal cracks connecting adjacent flexural cracks were detected, indicating a generally stable bond between the printed layers.

7.4 Modeling of bending capacity

To evaluate the bending behavior of the investigated T-beam, the flexural capacity was determined using a sectional analysis based on established reinforced concrete design principles. The approach follows the conventional sectional analysis methods proposed in Eurocode 2 (Chapter 6.1) [41], adapted to account for the material behavior of CFRP reinforcement and based on the Bernoulli hypothesis, assuming a linear strain distribution over the cross-section height (Fig. 10). The calculation is based on the assumption of a linear strain distribution over the cross-section height. For the concrete in the compression zone, a parabolic–rectangular stress–strain relationship is assumed, while the CFRP reinforcement is modeled as a linear-elastic material up to failure (Fig. 10). Similar to established steel-reinforced concrete design approaches, the internal forces are determined from

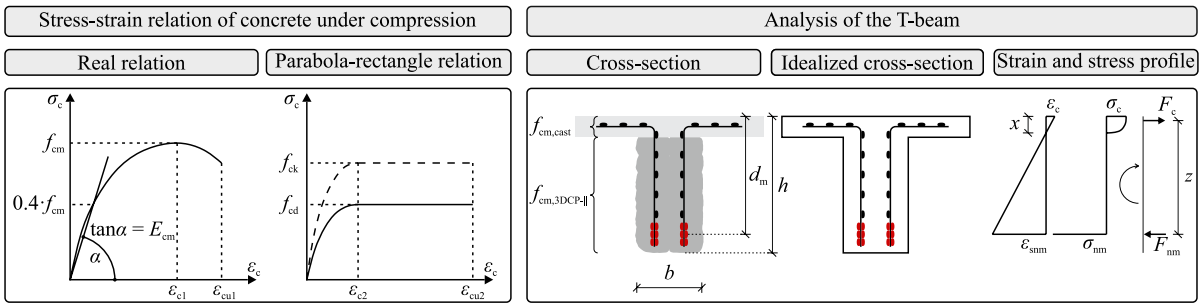


Fig. 10 (left) Schematic representation of the stress strain relation of concrete under compression; (right) Cross-section with stress distribution

equilibrium between compressive and tensile stresses at the cross-sectional level. Based on this, the bending capacity is evaluated using an iterative analysis procedure. The neutral axis position is varied iteratively, and for each iteration a corresponding strain state is defined, from which the stresses in the concrete and reinforcement are derived. The resulting internal forces are calculated, and equilibrium between compressive (F_c) and tensile (F_{nm}) forces is verified. The position of the neutral axis is adjusted until force equilibrium is achieved. Based on the resulting equilibrium state, the bending moment is determined. The ultimate load-bearing capacity corresponds to the maximum moment that can be sustained while satisfying the material limits.

The input parameters adopted for the analysis are summarized in Table 3. For the compressive strength and the modulus of elasticity, the material parameters of the cast concrete ($f_{cm,cast}$, $E_{cm,cast}$) were used for the cast plate in the compression zone, whereas the properties determined for the 3D-printed concrete ($f_{cm,3DCP-II}$, $E_{cm,3DCP-II}$) were adopted for the printed regions of the cross-section.

The analysis yields a maximum moment of 27.0 kNm, which deviates by less than 7% from the experimentally determined value. Consistent with the experimental observations, the calculations indicate that failure is governed by the longitudinal reinforcement reaching its ultimate strain. The presented proof-of-concept demonstrates that the bending capacity of multimodally fabricated concrete members can be predicted with good accuracy using established sectional analysis approaches when appropriate material properties are considered.

Table 3 Material characterisation of the T-beam

beam geometry		Mean
effective depth	d	200 mm
beam width	b	120 mm
Longitudinal reinforcement [48]		
cross-sectional area per yarn [1]	A_{nm}	3.62 mm^2
amount of yarns	n	12
total reinforcement area	$A_{nm,total}$	43.4 mm^2
reinforcement ratio	ρ_l	0.16%
tensile strength	f_{nm}	3221 N/mm^2
modulus elasticity	E_{nm}	244,835 N/mm^2
ultimate strain	ϵ_{nm}	13.2‰
Concrete		
mean strength	$f_{cm,cast,cyl}$	62 N/mm^2
	$f_{cm,3DCP-II}$	59.7 N/mm^2
mean strength	$E_{cm,cast}$	26,556 N/mm^2
	$E_{cm,3DCP-II}$	24,881 N/mm^2

[1] filament cross-sectional area without epoxy impregnation

8 Behavior under shear–Shear beams

8.1 Motivation

While the flexural behavior of reinforced 3D-printed concrete members can generally be predicted using established sectional analysis approaches, Sect. 3 has shown that existing shear design models are not directly transferable to digitally fabricated concrete members. In particular, interlayer bonding, crack propagation, and the reinforcement strategy significantly influence the shear load transfer. Since the shear resistance is governed by the printed web region, the experimental investigations were

conducted on fully 3D-printed CFRP-reinforced concrete beams. This enabled the governing shear transfer mechanisms to be investigated without the influence of the cast flange used in the multimodal structural members and provided the basis for evaluating the applicability of existing shear design approaches.

8.2 Shear reinforcement configurations

Beams with different shear reinforcement configurations (Fig. 11) were manufactured and tested under three-point bending. The investigated configurations comprised members with (0) no shear reinforcement, (1) a single L-shaped CFRP grid, (2) two L-shaped CFRP grids placed directly adjacent to each other, and (3) two L-shaped CFRP grids with a spacing of 10 mm in the cross-sectional direction (Fig. 11). These configurations were selected to systematically evaluate the influence of reinforcement arrangement on the bond and anchorage behavior between 3DCP and CFRP reinforcement. In configuration (0), the load-bearing behavior of unreinforced printed concrete was assessed. In configuration (1), the reinforcement is fully embedded in concrete from both sides, ensuring optimal bond conditions. In configuration (2), the CFRP grids are in direct contact with each other, resulting in a reduced concrete contact area per strand and consequently less favorable bond conditions, as the reinforcement is only partially embedded in concrete. In configuration (3), the spacing between the grids allows the reinforcement to be embedded from both sides; however, adequate bond conditions depend on the ability of the fresh concrete to flow between the reinforcement elements during the printing process. All specimens were reinforced longitudinally using a CFRP rebar with a diameter of 8 mm from the manufacturer *solidian* [56]. The specimens were fabricated by depositing a single concrete filament on either side of the shear reinforcement, with a nominal filament width of approximately 40 mm and a layer height of 15 mm. The beams had nominal dimensions of 1500 mm in length, 80 mm in width, and 220 mm in height (Fig. 11). Due to process-related deviations inherent to 3DCP, the actual dimensions varied slightly. A detailed overview of all specimens and their geometrical properties is provided in Table 4.

As a reference, one cast beam is considered to demonstrate the influence of the fabrication process. This specimen was part of a separate test series conducted at the same laboratory and reported in [57]. The cast beam was reinforced with shear reinforcement configuration (1) and longitudinally reinforced with two (instead of one) CFRP rebars (Ø8 mm)—the same rebar type as in the other beams. The details of the specimen (B-L-cast) are summarized in Table 4.

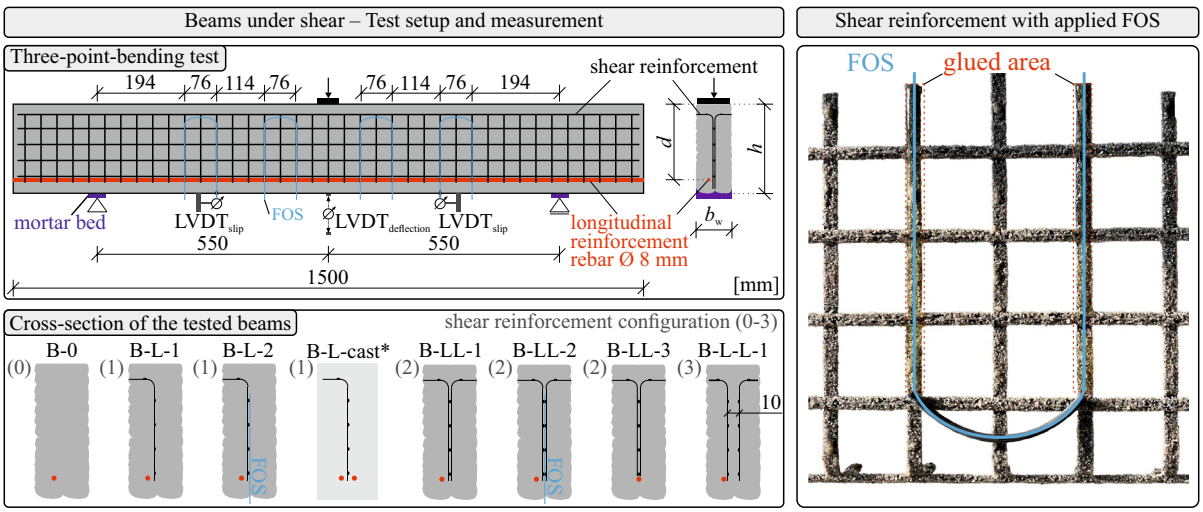


Fig. 11 Shear beams: test setup and overview of the analysed specimens

Table 4 Overview of the specifications of the shear beams

Codification	shear reinforcement			ρ_l	b_w	d	h	age	λ	F_{max}	V_{max}	$V_{max}/(b_w \cdot d)$	w_{max}
	configuration	n	a_{snm} [mm^2/m]	[%]	[mm]	[mm]	[mm]	[days]	[–]	[kN]	[kN]	[N/mm^2]	[mm]
B-0	(0)	–	0	0.37	75	182	217	19	3.0	13.5	6.8	0.5	3.2
B-L-1	(1)	1×*Q95*	95	0.33	83	186	220	19	2.9	35.9	18.0	1.1	11.1
B-L-2	(1)	1×*Q95*	95	0.28	96	190	221	20	2.9	34.8	17.4	1.0	9.2
BS-cast*	(1)	1×*Q95*	95	0.52	103	189	219	30	2.9	68.7	34.4	1.8	10.3
B-LL-1	(2)	2×*Q95*	190	0.32	84	186	219	19	2.8	51.1	25.6	1.5	12.7
B-LL-2	(2)	2×*Q95*	190	0.29	95	183	218	20	3.0	42.4	21.2	1.2	8.2
B-LL-3	(2)	2×*Q95*	190	0.33	80	188	195	20	2.9	50.2	25.1	1.6	12.2
B-L-L-1	(3)	2×*Q95*	190	0.29	93	185	222	19	2.9	63.7	31.9	1.8	12.8

n: Amount of shear reinforcement (L-profiles)

*Data from [57]

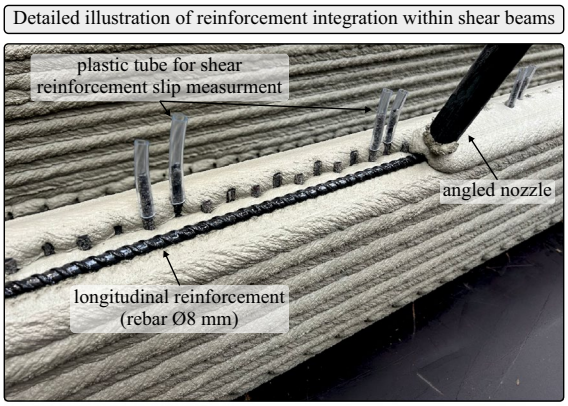


Fig. 12 Production of the shear beams

8.3 Fabrication

The fabrication process followed the procedure described in Sect. 4.1. In contrast to the previously presented elements, however, these specimens were produced exclusively using 3DCP, eliminating the influence of a cast base plate while focusing on the critical beam region with reduced anchorage conditions. The beams were printed layer-wise along the shear reinforcement using a nozzle angle of 20° and a printing speed of 100 mm/s. After 12 layers, the printing process was briefly interrupted to integrate the longitudinal CFRP reinforcement by embedding it into the fresh concrete (Fig. 12).

Although positioning the rebar centrally within the cross section would have minimized torsional effects, the longitudinal reinforcement was intentionally placed adjacent to the shear reinforcement to enable slip measurements, with individual CFRP strands extending from the beam (Fig. 12). Subsequently, the printing process was continued to achieve the target geometry. Additionally, one reference beam (B-LL-3) was produced with centrally positioned longitudinal reinforcement to investigate the influence of longitudinal reinforcement placement. After fabrication, all specimens were covered with foil to minimize moisture loss.

8.4 Test-setup and measurement

As shown in Fig. 11, the beam specimens were tested under three-point bending with a span of 1.1 m, resulting in a shear span-to-depth ratio $\lambda = 2.9$. To ensure uniform load transfer and to prevent torsional effects during testing, mortar beds were applied at the load introduction points to compensate for surface irregularities of the printed concrete (Fig. 11). The vertical load was applied using a hydraulic actuator, with the applied force monitored by load cells integrated into the loading system. The tests were conducted under deformation control at a midspan displacement rate of 1 mm/min. The beams were supported on one fixed and one movable roller support (Fig. 11). For the measurement of the overall structural response, LVDTs were installed at midspan to continuously record vertical deflections. In addition, the slip of the shear reinforcement was measured at four locations along the beam. For this purpose, plastic tubes were embedded within the printed concrete

and connected to the shear reinforcement (Fig. 12), enabling the displacement of the reinforcement to be recorded using LVDTs. Furthermore, deformation behavior and crack development were monitored using a photogrammetric measurement system based on digital image correlation (DIC). A stochastic speckle pattern was applied to one side of the beam, and measurements were carried out using the ARAMIS 2D DIC system from *Zeiss*. The monitored side corresponds to the face containing the longitudinal reinforcement. Additionally, two beams (B-L-2; B-LL-2) corresponding to configurations (2) and (3) were instrumented with fiber optic sensors (FOS) attached to the shear reinforcement (Fig. 11), providing detailed insight into the load transfer mechanisms of the CFRP grid reinforcement during testing. The sensors were glued to the reinforcement using a special adhesive, as described in [58, 59].

For material characterisation, prism specimens were produced during the fabrication process for material characterization of both cast and 3D-printed concrete. Compressive and flexural tensile strengths were determined in accordance with [52]. The cast concrete exhibited a mean compressive strength of $f_{cm,cast}$ = 47.1 N/mm^2 and a mean flexural tensile strength of $f_{ctm,cast}$ = 6.8 N/mm^2. For the 3DCP, compressive and flexural tensile tests carried out parallel to the printing direction, delivered mean values of $f_{cm,3DCP\text{-}\parallel}$=43.7 N/mm^2 and $f_{ctm,3DCP\text{-}\parallel}$=6.7 N/mm^2, respectively.

8.5 Results

8.5.1 Failure mode and crack patterns

Figure 13 illustrates the crack patterns of all tested beams. In each specimen, a dominant shear crack developed, which is highlighted in red. Overall, the specimens exhibited comparable structural behavior, with differences primarily related to the amount and configuration of shear reinforcement. The reference beam without shear reinforcement (B-0) showed the lowest crack density. Initially, flexural cracks formed in the midspan region. With increasing load, these cracks propagated and widened. At the ultimate load (F_{max} = 13.5 kN), the outermost crack propagated abruptly towards the load introduction point, resulting in a flexural–shear failure. Additionally, minor horizontal cracks were observed at the level of the

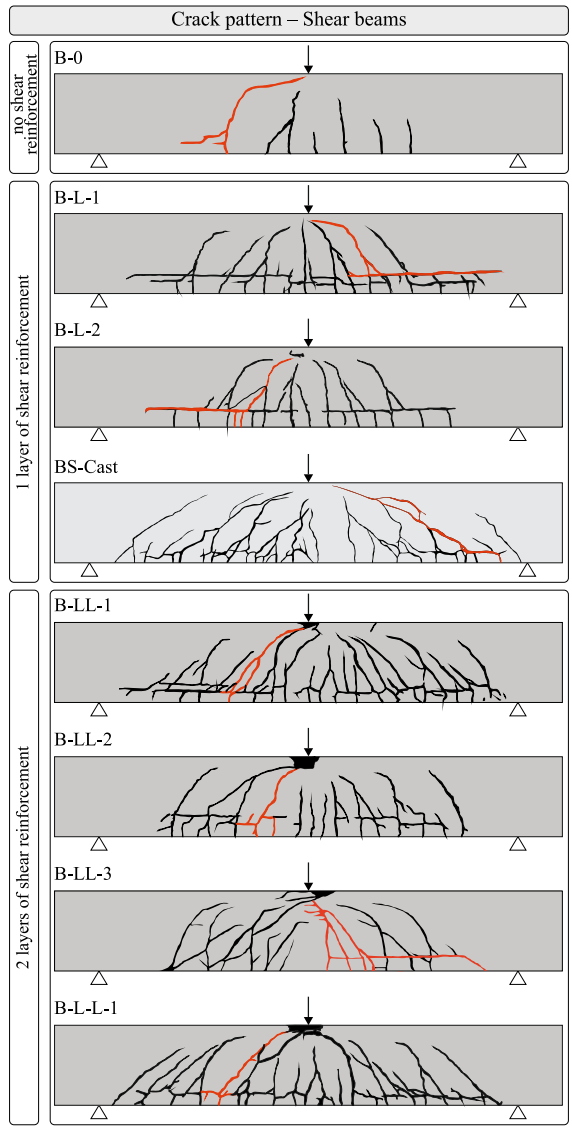


Fig. 13 Crack pattern of the shear beams

longitudinal reinforcement, connecting to the critical crack, although these were not strongly pronounced.

For the specimens with shear reinforcement, a clear influence of the reinforcement amount on the load-bearing capacity can be observed. Beams with a single layer of shear reinforcement (B-L-1: F_{max} =35.9 kN; B-L-2: F_{max} =34.8 kN) reached lower ultimate loads compared to beams with two layers of shear reinforcement (B-LL-1: F_{max} = 51.1 kN; B-LL-2: F_{max} = 42.4 kN; B-LL-3: F_{max} = 50.2 kN). This demonstrates the increased shear capacity resulting

from the use of multiple reinforcement layers. A noticeable difference in ultimate load was observed between specimens B-LL-1 and B-LL-2, despite having identical reinforcement configurations. This discrepancy can be attributed to the application of FOS on the shear reinforcement of specimen B-LL-2. The sensors were attached to the reinforcement grid using an adhesive, which altered the surface condition of the previously sanded strands, and thereby affecting the bond and anchorage behavior. In contrast, for beams with a single layer of shear reinforcement, no significant influence of the FOS instrumentation on the structural response was observed.

Furthermore, it can be observed that specimens with a single layer of shear reinforcement (B-L-1 and B-L-2) exhibited fewer cracks and, consequently, larger crack spacing compared to beams with two layers of shear reinforcement. In addition, the cast beam (BS-cast), also reinforced with a single layer, showed a higher crack density than the corresponding 3D printed beam with the same reinforcement configuration. This may indicate better bond conditions between reinforcements and surrounding concrete. However, it should be noted that the cast beam had a longitudinal reinforcement ratio nearly twice as high as that of the 3DCP beams, which also influences the cracking pattern.

8.5.2 Crack pattern development

All specimens with shear reinforcement failed in flexural shear and exhibited a ductile structural response. The procedure of the three-point-bending test is illustrated for beam B-LL-1 in Fig. 14.

Initially, a limited number of flexural cracks formed in the midspan region up to approximately one-third of the ultimate load. These cracks propagated steeply towards a height of about three-quarters of the beam depth (Fig. 14). Between 30–50% of the ultimate load, the existing flexural cracks widened slightly, while additional cracks developed between them with a flatter inclination. During this phase, initial horizontal cracks were observed in some specimens, predominantly forming at the interface between the last and the second-to-last printed layers, rather than at the level of the longitudinal reinforcement. With further load increase (50–85% of the ultimate load), additional cracks

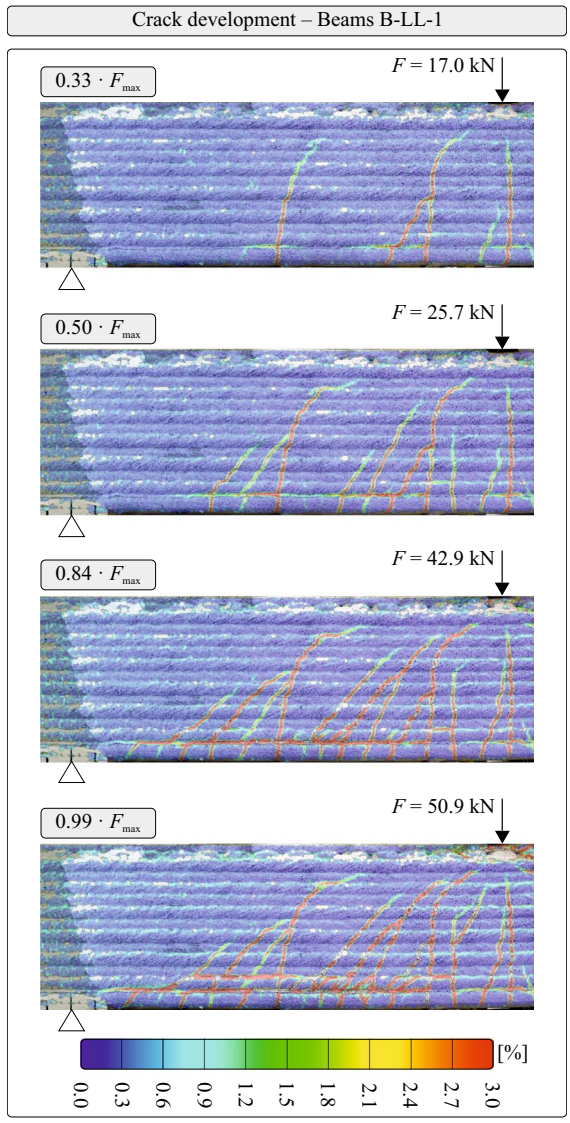


Fig. 14 Detailed demonstration of the crack development

formed, and existing cracks continued to widen. At approximately 85% of the ultimate load, more pronounced horizontal cracking developed along the level of the longitudinal reinforcement. At ultimate load, a dominant shear crack formed, propagating from the load introduction point towards the level of the longitudinal reinforcement and subsequently extending towards the support region, leading to failure.

It was observed that the cast beam (BS-cast) exhibited a similar overall behavior; however, the critical shear crack developed at a flatter

inclination, propagating more directly from the load introduction point towards the support. Although small horizontal cracks along the longitudinal reinforcement were observed, these were not connected to the critical shear crack.

8.5.3 Evaluation of the FOS

To investigate the activation and strain distribution of the shear reinforcement during loading, two beams (B-L-2 and B-LL-2) were instrumented with fiber optic sensors (FOS) [60, 61]. For this purpose, four optical fibers, always distributed over two CFRP strands, were bonded to the CFRP shear reinforcement profiles prior to the printing process, as illustrated in Fig. 11. The sensor application and bonding procedure were carried out according to the methodology described in [62]. Subsequently, the specimens were fabricated using the multimodal manufacturing process.

For each beam, strain measurements were evaluated at eight cross-sections along the beam length, corresponding to the locations shown in Fig. 15. Due to local damage of the optical fibers, one of the sensors in both specimens failed before testing. The strain distribution presented for specimen B-L-2 corresponds to a load level of $F = 25.7$ kN ($0.74 \cdot F_{max}$), which corresponds to the final load stage at which all three sensors were still operational. Figure 15 presents both the measured strain distribution along the reinforcement and the strain–time response during the complete loading process. The results reveal localized strain concentrations in the regions intersected by the critical shear crack, indicating a progressive activation of the CFRP shear reinforcement during crack development. Maximum reinforcement strains of up to approximately 7‰ were measured.

In contrast to B-L-2, no additional sensor failure occurred in specimen B-LL-2, allowing continuous strain monitoring throughout the complete test. However, a direct quantitative comparison between B-LL-2 and the corresponding reference specimen without FOS instrumentation (B-LL-1) is not possible, as specimen B-LL-2 exhibited a reduced load-bearing capacity. This reduction is attributed to the influence of the sensor application on the bond conditions of the CFRP reinforcement. Nevertheless, the FOS measurements clearly demonstrate that the shear reinforcement is activated during loading and contributes to the load transfer after shear crack formation.

8.5.4 Effect of the reinforcement layout

Figure 16 (left) presents the load-deformation behavior of five 3D printed beams with different shear reinforcement configurations. Due to process-related variations inherent to 3DCP, slight differences in web width and specimen height were observed among the specimens (Table 4). To ensure comparability, the results are therefore evaluated in terms of normalized shear stress $V/(b_w \cdot d)$. All specimens exhibited a similar initial response prior to cracking. Following crack initiation, a noticeable reduction in stiffness was observed; however, the load continued to increase until reaching the ultimate capacity. All specimens exhibited splitting cracks along the interface between the adjacent concrete filaments surrounding the shear reinforcement, indicating progressive bond deterioration and slip of the shear reinforcement (Fig. 16).

Specimens reinforced with two layers of shear reinforcement showed a higher stiffness compared to those with a single layer (B-L-1). The reference beam without shear reinforcement (B-0-1) exhibited the lowest load-bearing capacity, reaching an ultimate load of 13.5 kN at a deflection of 3.2 mm. In contrast, beam B-L-1 with one layer of shear reinforcement achieved an ultimate load of 35.9 kN and a deflection of 11.1 mm, demonstrating the significant contribution of shear reinforcement to the structural performance. The beams B-LL-1 ($F_{max} = 51.1$ kN; $w_{max} = 12.7$ mm) and B-LL-3 ($F_{max} = 50.2$ kN; $w_{max} = 12.2$ mm), both reinforced with two layers of CFRP grids, exhibited comparable behavior. The specimen B-LL-3, with centrally positioned longitudinal reinforcement, exhibited a slightly higher stiffness, indicating that the influence of the longitudinal reinforcement position is negligible for this test series. A notable increase in load-bearing capacity was observed for beam B-L-L-1 with two CFRP grids arranged with a spacing of 10 mm. This specimen reached the highest ultimate load of 63.7 kN at a deflection of 12.8 mm. The improved performance can be attributed to enhanced anchorage conditions and increased bond area of the shear reinforcement.

These observations are further supported by Fig. 16 (right), which illustrates the normalized load-slip behavior of the shear reinforcement. For each

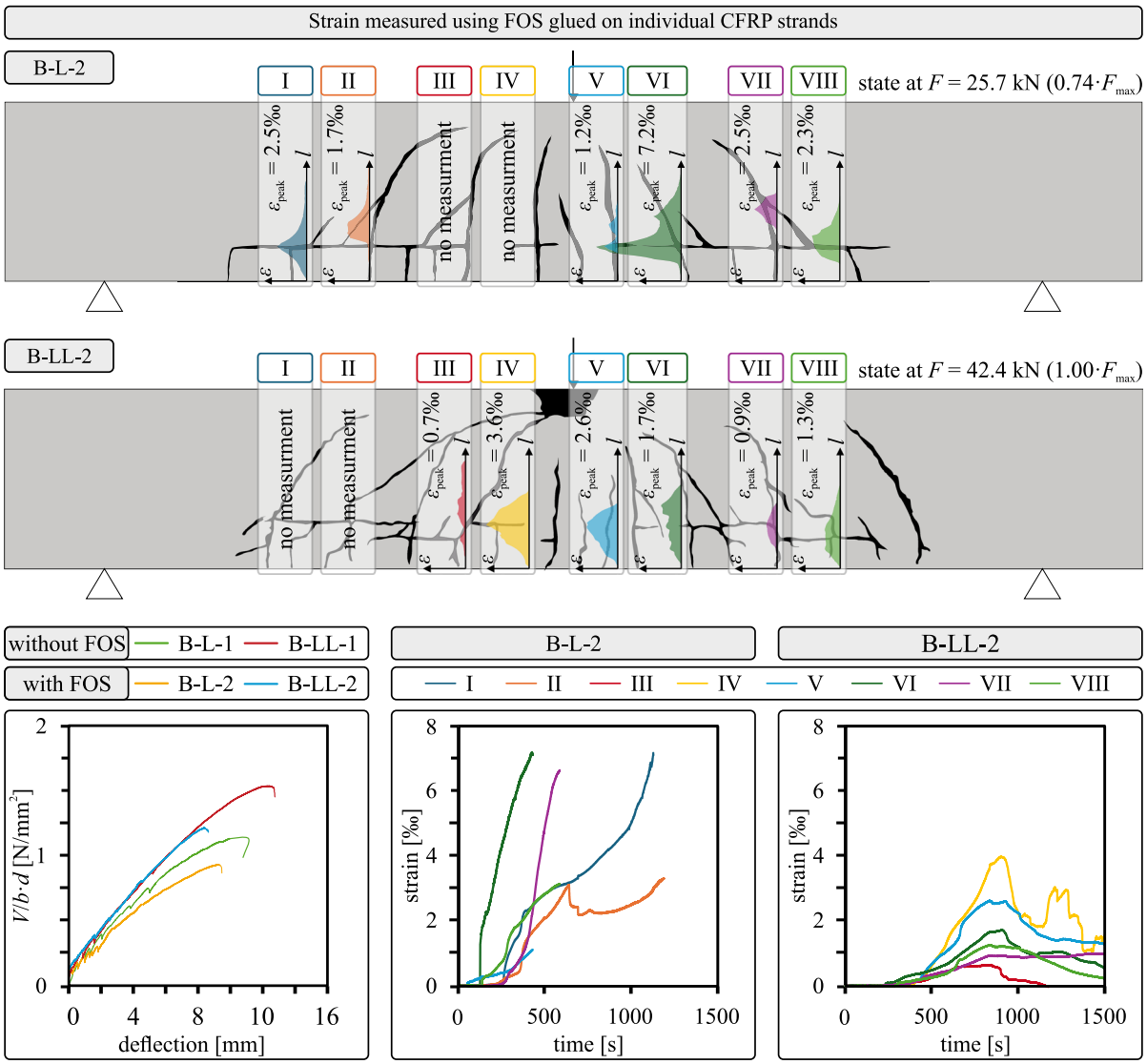


Fig. 15 Evaluation of the strain distribution in the CFRP shear reinforcement measured using fiber optic sensors (FOS) for specimens B-L-2 and B-LL-2

beam, the critical shear crack intersecting one of the instrumented CFRP strands was identified (Fig. 13). The slip response of this strand, which exhibited the highest displacement among the measured locations, is presented in Fig. 16. The results confirm that improved bond and anchorage conditions lead to more effective activation of the shear reinforcement and, consequently, to higher load-bearing capacities.

8.5.5 Influence of the manufacturing approach

To provide a qualitative comparison between cast and 3D-printed specimens, Fig. 17 compares the normalized load–deflection response of beam specimens with comparable reinforcement configurations. For this purpose, additional cast and 3D-printed beams from another experimental series conducted at the Institute of Structural Concrete at RWTH Aachen University were included in the evaluation [57]. These specimens were manufactured and tested under

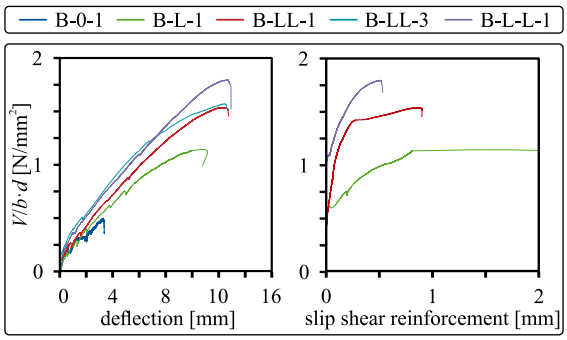


Fig. 16 Shear beams—effect of the reinforcement layout

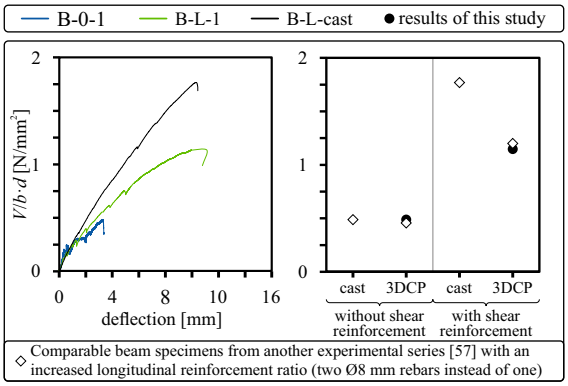


Fig. 17 Shear beam—influence of the manufacturing process

comparable conditions to the beams investigated in the present study. However, it should be noted that the specimens from the additional series contained a higher longitudinal reinforcement ratio, consisting of two Ø8 mm rebars instead of one. Therefore, the comparison should be regarded as a qualitative benchmark rather than an isolated assessment of the manufacturing process.

The results shown in Fig. 17 indicate that beams without shear reinforcement exhibit almost no difference between cast and 3D-printed fabrication. In contrast, significant differences were observed for beams with shear reinforcement. The cast beam BS-cast reached a normalized shear stress of 1.8 N/mm^2, whereas the 3D-printed beam B-L-1 achieved only 1.1 N/mm^2, corresponding to a reduction of approximately 39%. Part of this difference is attributed to the higher longitudinal reinforcement ratio of the cast reference specimen. However, the additional 3D-printed beam from [57] with the same increased longitudinal reinforcement ratio reached a normalized shear stress of only 1.2 N/mm^2, corresponding to an increase of approximately 9% compared to specimen B-L-1. This indicates that the increased longitudinal reinforcement ratio alone cannot explain the observed difference in shear resistance and suggests that the manufacturing process has a significant influence on the structural response. The reduced performance of the 3D-printed specimens can therefore primarily be attributed to the altered bond and anchorage conditions of the shear reinforcement resulting from the layer-wise fabrication process. In contrast to cast concrete, extrusion-based fabrication introduces interfaces between adjacent concrete filaments and locally reduced confinement around the reinforcement, impairing the stress transfer between CFRP reinforcement and concrete. Consequently, the anchorage behavior of the shear reinforcement is identified as one of the governing parameters influencing the shear resistance of reinforced 3D-printed concrete members, which is consistent with the bond investigations presented in Sect. 6.

8.6 Modeling of shear capacity

8.6.1 Load transfer mechanisms

The shear behavior of reinforced concrete members is governed by a combination of interacting load transfer mechanisms. In beams without shear reinforcement, shear forces are resisted by the uncracked compression zone, aggregate interlock along crack surfaces, dowel action of the longitudinal reinforcement and residual tensile stresses at the crack tip. In members with shear reinforcement, an additional mechanism is activated. Inclined shear cracks intersect the reinforcement, leading to tensile forces in the shear reinforcement, which contributes to the load-bearing capacity by bridging the crack. The overall shear resistance can therefore be described as the superposition of the concrete contribution and the reinforcement contribution. An overview of the governing load transfer mechanisms is provided in [48].

In the case of 3DCP, these mechanisms are influenced by the anisotropic material behavior and the layer-wise deposition process. In particular, reduced tensile strength perpendicular to the printing direction and modified bond conditions affect crack formation,

crack propagation, and the activation of shear reinforcement. As a result, both the concrete contribution and the effectiveness of the shear reinforcement are expected to differ from conventional reinforced concrete.

8.6.2 *Guideline-based prediction of the shear capacity*

For the prediction of the shear capacity of non-metallic reinforced concrete members, several design approaches and guidelines are available [63, 64]. Most existing approaches, such as ACI 318 [65], Eurocode 2 [41], and DAfStb-Bulletin 660 [44], describe the total shear resistance V_R as the sum of the concrete contribution $V_{R,c}$ and the shear reinforcement contribution $V_{R,s}$:

$$V_R = V_{R,c} + V_{R,s} \tag{1}$$

In conventional design approaches, the concrete contribution is generally determined using semi-empirical formulations calibrated against extensive experimental databases of cast concrete members. For 3DCP, however, such comprehensive experimental datasets are currently not available, and the direct transferability of existing empirical formulations cannot be assumed.

DAfStb-Bulletin 660 determines the concrete contribution to the shear resistance of members without shear reinforcement using the following equation:

$$V_{R,c} = \left[C_{R,c} \cdot k \cdot k_\lambda \cdot \left(100 \cdot \rho_l \cdot \left(E_{nml}/E_s\right) \cdot f_{ck}\right)^{1/3} \right] \cdot b_w \cdot d \tag{2}$$

where $C_{R,c}$ is an empirical coefficient, k_λ accounts for the shear slenderness, k represents the size effect factor, ρ_l is the longitudinal reinforcement ratio, E_{nml}/E_s describes the stiffness ratio between non-metallic and steel reinforcement, f_{ck} is the characteristic value of the cylinder compressive strength of the concrete, and b_w and d denote the web width and effective depth, respectively. Depending on the intended level of assessment, $C_{R,c}$ takes values of 0.103, 0.155 and 0.219 for design, characteristic and mean-value predictions, respectively. Although the mean-value prediction in this study is based on the measured mean concrete strength, the empirical formulation remains expressed in terms of f_{ck}; therefore, f_{ck} is retained in Eq. (2) and derived from f_{cm} as $f_{ck} = f_{cm} - 8$ MPa, in accordance with DAfStb Bulletin 660.

Based on this, the predicted concrete contribution amounts to $V_{R,c} = 13.1$ kN. In comparison, the experimentally determined shear capacity is only $V_{max} = 6.8$ kN, indicating a significant overestimation by the guideline. This discrepancy is attributed to the layer-wise fabrication process and the resulting anisotropic material behavior of the 3DCP. In particular, the interlayer bond between adjacent filaments and the reduced bond conditions in the vicinity of the longitudinal reinforcement are assumed to influence the governing shear transfer mechanisms. Furthermore, the empirical parameters of DAfStb-Bulletin 660 were calibrated for conventionally cast concrete and have not yet been validated for digitally fabricated concrete members.

For the investigated specimen, the empirical factor $C_{R,c} \cdot k_\lambda$ according to the guideline amounts to 0.62. However, based on the experimental results, a significantly lower value of $C_{R,c} \cdot k_\lambda = 0.29$ is required to achieve agreement with the findings of the present experimental study. This indicates that the concrete contribution according to existing design approaches cannot be directly transferred to 3D-printed concrete members without further adaptation.

It should be noted that a reliable recalibration of the empirical factor would require an extensive experimental database comprising a large number of systematically varied test specimens.

While the value derived from the investigated beam provides an indication of the reduced concrete contribution in the present study, it cannot be considered a generally applicable calibration parameter. Consequently, purely empirical recalibration approaches would require considerable experimental effort. Alternatively, mechanics-based models may provide a more reliable approach for predicting the shear capacity of 3DCP members.

8.6.3 *Extension of the shear crack propagation theory to 3DCP*

As mentioned before, there still is a need for physics-based models describing the structural behavior of 3DCP members. For this reason, an extension of the *Shear Crack Propagation Theory* (SCPT) [18] is proposed. The SCPT, in its original formulation, provides a holistic framework for evaluating the shear

resistance of slender reinforced concrete members without shear reinforcement. It describes shear failure as a progressive crack propagation process governed by the stress state at the crack tip and the load transfer within the concrete tooth, defined as the concrete body between two adjacent cracks acting as a cantilever beam transferring shear between the compression and tension chord of the member, as shown in Fig. 18. Being a holistic model, the SCPT further considers compatibility and equilibrium requirements, different constitutive laws, as well as all the aforementioned shear transfer mechanisms. While the SCPT has shown good predictive capabilities for conventionally cast reinforced concrete, its direct application to 3DCP members is limited due to the presence of layered interfaces and anisotropic material behavior introduced by the printing process.

To account for these fabrication-induced characteristics, the SCPT framework was extended by incorporating the possibility of interface delamination along printed layer boundaries. Within the proposed approach, the propagation of the critical shear crack is tracked incrementally throughout the analysis, such that the position of the crack tip is continuously updated at each calculation step. Whenever the crack tip approaches a printed interface, the local biaxial stress state is evaluated in terms of the normal stress σ_{z0} and shear stress τ_0. Interface failure is evaluated using the mixed-mode criterion proposed by [66]:

$$\Phi_{\text{int}} = \left(\sigma_{z0}/t_{n0}\right)^2 + \left(\tau_0/t_{t0}\right)^2 \tag{3}$$

where t_{n0} and t_{t0} denote the tensile and shear strengths of the interface, respectively, and must be determined experimentally. Delamination is assumed to initiate once $\Phi_{\text{int}} > 1.0$.

Following interface failure, a delaminated region develops along the corresponding layer boundary.

The extent of this delamination increases as the interface stresses exceed the failure criterion, and it is therefore proportional to Φ_{int}. Within the SCPT framework, this directly affects the effective geometry of the aforementioned concrete tooth, leading to a reduction of its section modulus W_c, as shown in Fig. 18. The reduction in W_c, in turn increases the vertical stress σ_{z0} at the crack tip, which is caused by the clamping moment M_{CA} of the concrete tooth (Fig. 18):

$$\sigma_{z0} = M_{\text{CA}}/W_{\text{c}} \tag{4}$$

Consequently, interface degradation and crack propagation become mutually coupled processes: progressive delamination leads to higher stress concentrations, which may further accelerate crack growth until no equilibrium state can be maintained and shear failure occurs.

The delamination state is retained throughout the incremental analysis procedure, enabling the accumulation of interface damage over successive load steps. In addition, the interface parameters can be adapted to represent varying interlayer bond qualities resulting from different printing conditions, time intervals between deposited layers, or intentionally weakened interfaces.

Initial comparisons with experimental investigations on the shear behavior of 3DCP beams without shear reinforcement shown in [20] indicate that the extended approach is capable of reproducing the observed reduction in shear resistance with satisfactory agreement, yielding a mean prediction accuracy of 1.01 and a coefficient of variation of 0.16.

In principle, the proposed framework has also been extended to members with shear reinforcement. For

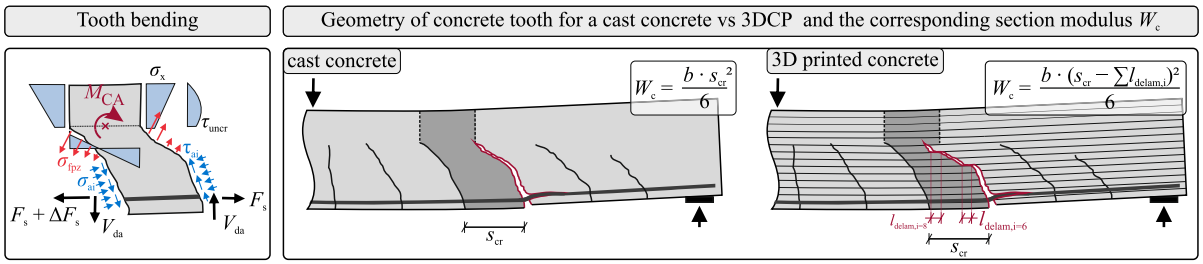


Fig. 18 (left) Forces acting on a concrete tooth and the resulting clamping moment M_{CA}; (right) Geometry of concrete tooth for a cast vs 3D printed concrete member and the corresponding section modulus W_{c}

CFRP grids, which consist of orthogonally arranged strands in longitudinal and transverse directions, the model accounts for strands that intersect the inclined shear crack. Each crossing yarn contributes through two primary mechanisms: dowel action and tensile force development. Dowel action is modeled for each yarn using a nonlinear force–displacement relationship suggested in [67] that accounts for the yarn's moment of inertia, inclination angle relative to the crack, and current stress level. Additionally, the tensile forces are calculated based on the crack opening at the yarn location and a corresponding bond stress model. These forces are then summed across all crossing strands, scaled by the number of grid layers, and integrated into the equilibrium equations alongside the existing concrete mechanisms.

However, a critical aspect of accurately modeling shear reinforcement in 3DCP members lies in the assumed bond stress-slip relationship, which, as shown before, fundamentally differs from that in conventionally cast concrete. This necessitates a 3DCP-specific bond stress model that accounts for the reduced mechanical interlock. Furthermore, the development of bond stress is highly dependent on the embedded length of the strands within the concrete matrix, which varies spatially depending on the yarn's position relative to the crack and the member geometry. The SCPT framework naturally provides the capability to compute these embedded lengths for each crossing yarn, enabling precise bond stress calculations. However, deriving a comprehensive bond stress-slip law applicable to the full range of embedded lengths requires a more extensive experimental characterization than that presented in Sect. 6. Such data would allow calibration of the bond model parameters, ensuring that the predicted tensile forces in the shear reinforcement remain realistic. This is therefore still subject of ongoing research.

8.6.4 Predicting the shear capacity of the conducted experimental series

For the reasons outlined above, a fully mechanics-based prediction of the investigated beam series using the extended SCPT framework alone is currently not feasible, as the experimental database required for the derivation and calibration of a reliable bond stress-slip model for CFRP reinforcement embedded in 3D-printed concrete is still limited. Therefore, a hybrid approach is adopted in the following, combining the physically based SCPT formulation for the concrete contribution $V_{R,c}$ with the provisions of the DAfStb-Bulletin 660 for evaluating the contribution of the shear reinforcement $V_{R,s}$.

The extended SCPT framework for 3D-printed concrete (Sect. 8.6.3) was used to determine the concrete contribution to the shear capacity of the beams B-0, B-L-1, B-LL-1 and B-L-L-1 in order to compare the influence of the different shear reinforcement layouts (Table 5). The calculations were performed using the parameters listed in Table 4. For specimen B-0, which did not contain shear reinforcement, the calculated shear capacity amounted to $V_{SCPT} = 7.4$ kN, corresponding to 1.09 times the experimentally determined value of $V_{exp} = 6.8$ kN. This result indicates a satisfactory agreement between prediction and experiment and suggests that the extended SCPT framework is capable of capturing the governing mechanisms of

Table 5 Overview of the shear capacities of the investigated beams and the corresponding contributions of concrete and shear reinforcement

Codification	n	V_{SCPT}	$V_{R,s}$	$V_{SCPT} + V_{R,s}$	V_{exp}	$(V_{SCPT} + V_{R,s}) / V_{exp}$
	[–]	[kN]	[kN]	[kN]	[kN]	[–]
B-0	–	7.4	–	7.4	6.8	1.09
B-L-1	1×*Q95*	7.6	10.8	18.4	18.0	1.02
B-LL-1	2×*Q95*	7.7	16.4	24.1	25.6	1.07
B-L-L-1	2×*Q95*	8.1	24.6	32.7	31.9	1.03

n: number of shear reinforcement (L-profiles)

V_{SCPT} contribution of the concrete in accordance with Sect. 8.6.3

$V_{R,s}$ contribution of the shear reinforcement

shear failure in 3D-printed concrete members without shear reinforcement.

According to the DAfStb-Bulletin 660, the contribution of the shear reinforcement $V_{R,s}$ is determined based on the effective reinforcement area and the tensile capacity of the reinforcement:

$$V_{R,s} = A_{nmw}/s \cdot z \cdot f_{nmw} \cdot \cot\theta \quad (5)$$

where A_{nmw} is the effective shear reinforcement area, f_{nmw} is the tensile strength of the CFRP reinforcement, z is the internal lever arm, and θ is the inclination of the critical shear crack.

However, the experimental investigations demonstrated that the shear behavior of the 3D-printed specimens is strongly influenced by the bond and anchorage conditions of the reinforcement, which are not explicitly considered in the conventional design formulation. In addition, the inclination θ and propagation of the critical shear crack were found to vary depending on the reinforcement configuration and the local crack development (Fig. 19). Consequently, a direct application of the guideline-based approach is not sufficient for the investigated 3DCP members.

Therefore, an adapted approach is proposed in the following, which explicitly accounts for the experimentally observed bond behavior and anchorage conditions of the individual CFRP strands. Following the additive shear resistance concept, the total shear resistance is finally assumed to consist of a concrete contribution determined using the extended SCPT framework and a reinforcement contribution derived from the experimentally determined bond behavior.

For this purpose, the critical shear crack observed in each beam was evaluated individually (Fig. 19). In all beams five CFRP strands were observed to intersect the critical crack and were therefore considered in the calculation. The effective bond length of each strand was defined as the distance between the crack intersection point and the free end of the reinforcement. For strands intersected by secondary cracks below the critical shear crack, the effective bond length was reduced accordingly to the distance between the reinforcement end and the first intersecting crack (highlighted in green in Fig. 19).

The transferable force of each CFRP strand was determined using the experimentally derived bond laws presented in Sect. 6, assuming a constant bond stress along the effective embedment length.

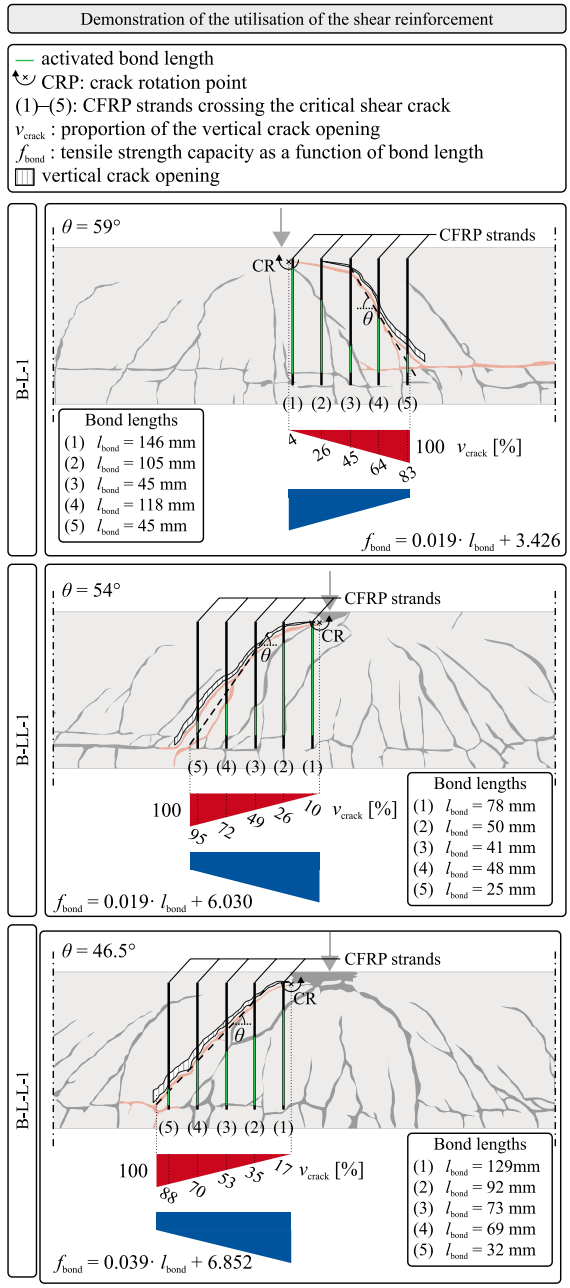


Fig. 19 Critical shear crack patterns of specimens B-L-1, B-LL-1 and B-L-L-1 with the intersecting CFRP strands and corresponding effective bond lengths

Furthermore, the activation of the reinforcement was related to the local crack opening. Based on the experimentally observed crack kinematics, a linear crack opening distribution was assumed between the

crack initiation point and the center of rotation (CR). Consequently, reinforcement strands located in the vicinity of the maximum crack opening exhibited the highest activation, while the activation decreased continuously towards the crack rotation point (Fig. 19). Accordingly, the transferable reinforcement force was determined as:

$$V_{R,s} = \sum v_{crack,i} \cdot f_{bond,i} \quad (6)$$

where $v_{crack,i}$ represents the activation factor of the individual CFRP strand depending on the local crack opening, and $f_{bond,i}$ denotes the transferable tensile force derived from the experimentally determined bond law for the corresponding embedment length (Fig. 19).

For specimens B-L-1 and B-L-L-1, full concrete embedding around the individual CFRP strands was assumed. In contrast, specimen B-LL-1, containing directly adjacent CFRP strands, was evaluated using a reduced bond capacity of 12%, as observed in the experiments presented in Sect. 6.

The proposed approach is based on the following simplifying assumptions:

- Constant bond stress along the effective embedment length,
- Full anchorage of the reinforcement within the compression zone,
- Formation of a single dominant shear crack, linear crack opening distribution between crack initiation and CR.

Figure 19 illustrates the critical shear crack patterns of specimens B-L-1, B-LL-1, and B-L-L-1 together with the corresponding CFRP strands intersecting the crack. The associated effective bond lengths used for the calculations are highlighted in green.

Table 5 summarizes the calculated concrete contribution V_{SCPT} obtained from the extended SCPT framework, the reinforcement contribution $V_{R,s}$ determined according to the proposed approach and the resulting total shear resistance. The comparison between calculated and experimentally determined shear capacities shows deviations of less than 9%, indicating that the proposed approach is capable of reproducing the shear behavior of the investigated beam series with satisfactory accuracy. However, the determination of the reinforcement contribution requires knowledge of the effective bond lengths and activation of the individual CFRP strands intersecting the critical shear crack. This again highlights the importance of physically based models capable of predicting both the crack propagation and the resulting activation of the reinforcement. Therefore, the further development of the extended SCPT framework represents a key prerequisite for the reliable prediction of the shear capacity of digitally fabricated reinforced concrete members.

9 Punching shear–large scale testing on a ribbed ceiling module

9.1 Motivation

To investigate the transferability of the previously studied shear mechanisms to structural scale, a large-scale punching shear test was conducted as a proof-of-concept on a ribbed ceiling module (Fig. 20). The module geometry is based on the modular ceiling system presented in [14, 22, 68] and represents a load-adapted ribbed slab configuration.

9.2 Specimen and fabrication

The ribbed ceiling module consists of a cast base plate and a 3D-printed ribbed substructure. The geometry includes a central column support region (Ø = 200 mm), an outer ring, and eight radial webs connecting both regions. The base plate has a diameter of 1500 mm and a thickness of 40 mm and was reinforced with two planar CFRP grids. The webs have a width of 60 mm and a height of 160 mm, resulting in a total structural height of 200 mm. Due to the radial arrangement of the webs, the CFRP shear reinforcement profiles intersect in the central region. As a result, only one web contains a continuous shear reinforcement profile passing through the core, while the remaining webs are reinforced up to the core boundary.

The specimen was fabricated using the multimodal process described in Sect. 4.1. The ribbed structure was 3D-printed directly onto the freshly cast plate. The printing process was carried out in a continuous sequence with a printing speed of 100 mm/s, a layer height of 15 mm, and a filament width of

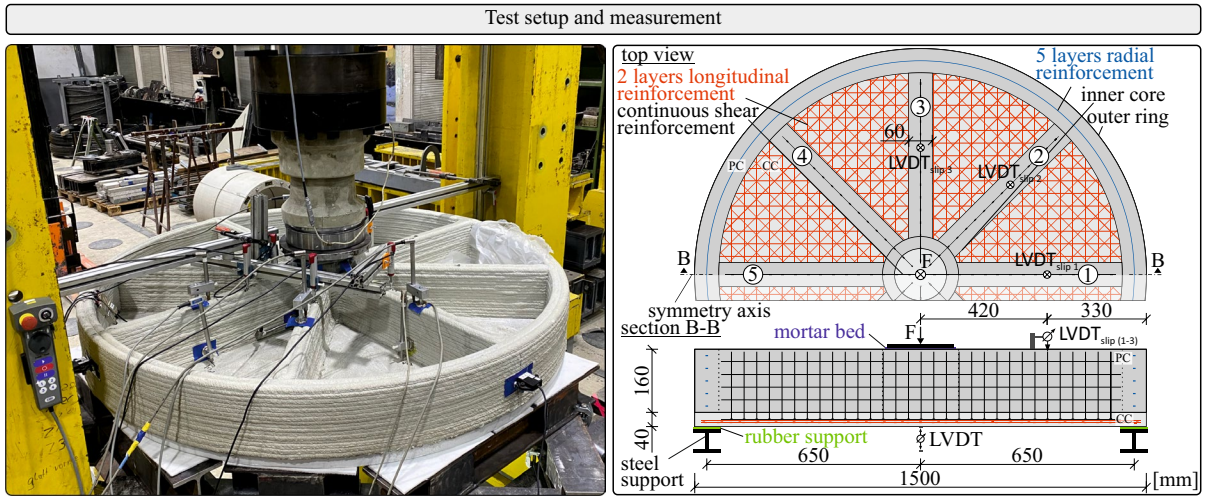


Fig. 20 Punching shear test setup for a ribbed ceiling module

approximately 30 mm. The webs were reinforced using CFRP profiles corresponding to shear reinforcement configuration (2). In addition, ring reinforcement consisting of multiple layers of CFRP strands (*solidian Q95*) was integrated in the outer ring. The detailed geometry and reinforcement layout of the specimen are shown in Fig. 20. After fabrication, the ceiling module was moistened, covered with polyethylene foil to minimize moisture loss, and tested after 33 days.

9.3 Test setup

To analyze the load-bearing behavior, the specimen was tested in an inverted punching shear setup (Fig. 20). The module was positioned with the cast side facing downward in an octagonal test frame and was supported continuously along its perimeter. To minimize friction and ensure uniform stress distribution, an 8 mm thick rubber layer was placed between the specimen and the steel support. The load was applied centrally over the inner core region (Ø = 200 mm) using a hydraulic actuator under displacement control at a rate of 1 mm/min.

Prior to failure, the loading process was briefly stopped in steps of 25 kN to allow for visual inspection. After reaching 200 kN, the specimen was loaded continuously until failure. In addition to measuring the vertical deflection at the midpoint, the slip of the shear reinforcement was monitored at three positions within the webs (①–③ in Fig. 20) using LVDTs.

9.4 Results

The observed failure was not governed by classical punching shear, but rather by a shear failure of the webs. Post-test inspection revealed splitting of the concrete along the CFRP shear reinforcement and pull-out of the shear reinforcement from the surrounding concrete (Fig. 21), indicating a bond- and anchorage-governed failure mechanism consistent with the results of the shear beam tests.

Pronounced shear cracks developed within the webs, while final failure was associated with local concrete crushing in the compression zone near the load introduction area. The failure of the individual webs was documented after testing by photographs and schematic crack patterns (Fig. 21). Initially, flexural cracks formed at the outer edge of the cast plate along the interface with the webs. These cracks propagated vertically into the outer ring and horizontally toward the inner core. From a load level of approximately 150 kN, crack extended into the printed webs. At advanced loading stages, partial detachment of the printed outer ring was observed at the interface with the cast plate. In addition, local spalling occurred at the upper edges of the webs adjacent to the ring,

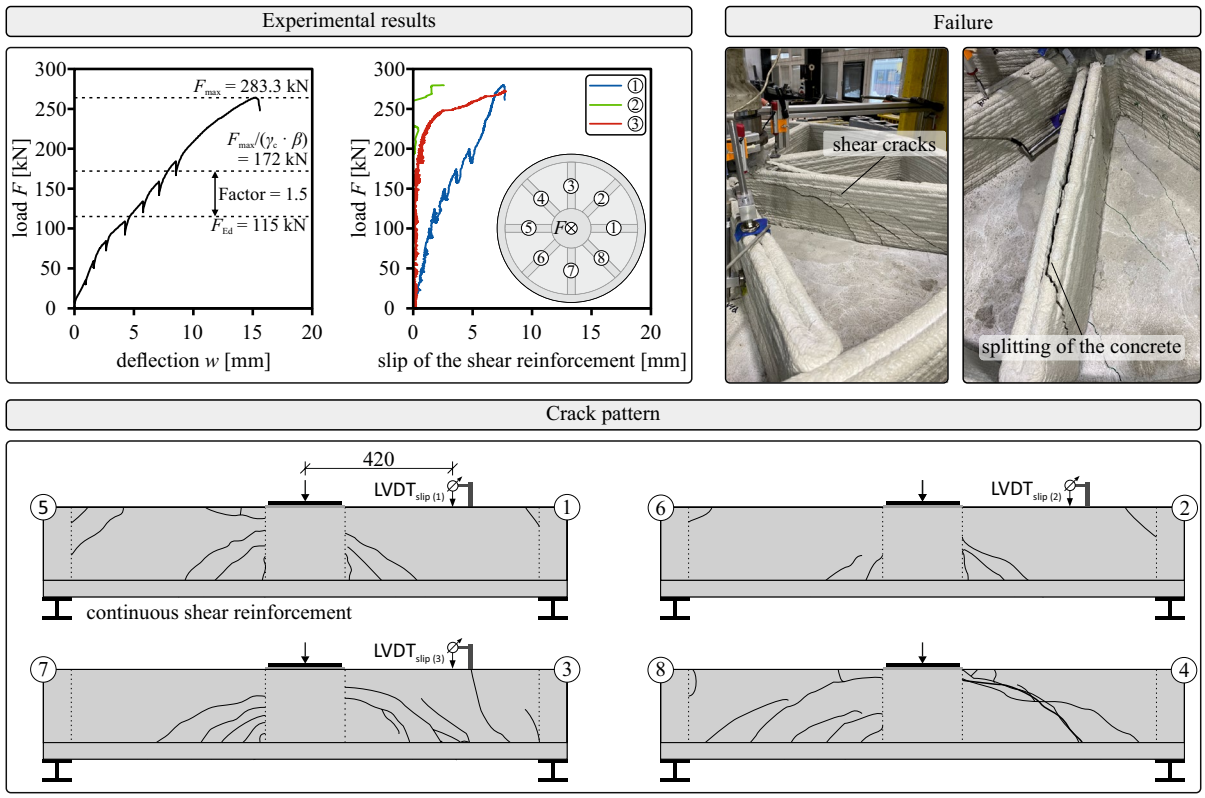


Fig. 21 (left) Load deformation behavior; (middle) load slip behavior of the shear reinforcement; (right) crack pattern of the printed webs after failure. (Fmax: ultimate reached load, F_{Ed}: required design load, $\gamma_c = 1.5$: safety factor, $\beta = 1.1$: coefficient for the punching shear resistance of internal columns)

indicating that the ring constrained the deformation of the webs and influenced the crack development.

The load–deformation response is shown in Fig. 21. The specimen reached an ultimate load of 283.3 kN (including self-weight) at a deformation of 15.5 mm measured at midspan. Up to a load of approximately 25 kN, only minor deformations were observed. This was followed by an approximately linear response up to about 100 kN. At higher load levels, a gradual reduction in stiffness occurred until failure. The load–slip behavior of the shear reinforcement is also presented in Fig. 21. The largest slip was observed in web ①, which contained the continuous reinforcement passing through the central core. Slip initiation in this web occurred at a relatively low load level of approximately 50 kN. In contrast, the reinforcement in webs ② and ③ exhibited slip initiation at significantly higher load levels, around 200 kN, increasing until failure. The measured slip behavior strongly depends on the location and development of shear cracks, highlighting the interaction between crack propagation and local bond conditions. For modeling such ribbed concrete members, mechanics-based approaches capable of describing both punching and shear-governed failure mechanisms are required. In the vicinity of the support region, existing punching shear models such as the *Punching Shear Response Theory* (PSRT) [69] may provide a suitable basis, as they describe the fracture kinematics through components of rotation and translation. For the ribbed outer region, however, the governing behavior is dominated by shear crack propagation within the webs. Consequently, approaches such as the SCPT, which explicitly account for crack propagation, crack friction, dowel action, and compression zone effects, are particularly suitable for describing the observed structural behavior of digitally fabricated ribbed concrete members.

9.5 Comparison with beam tests

To relate the large-scale ceiling module to the isolated shear beam tests, the structural response of the individual ribs is compared. As both specimens employ the same rib cross-section and CFRP shear reinforcement configuration, and failure occurred within the printed ribs, the comparison focuses on the governing shear behavior of the printed web. The maximum punching load of the ceiling module amounted to 283.3 kN, corresponding to an average shear force of approximately 35.4 kN per rib. This value exceeds the maximum shear resistance of the isolated beam B-LL-1 (25.6 kN), although both specimens employed the same CFRP shear reinforcement configuration.

Despite this difference in load-bearing capacity, both investigations exhibited the same governing failure mechanism. In both cases, failure was initiated by diagonal flexural shear cracking within the printed ribs, followed by crushing of the concrete in the compression zone. This indicates that the isolated beam tests captured the governing shear behavior of the printed ribs, while the ceiling module demonstrates the interaction of these mechanisms within a structural-scale component.

The higher shear resistance observed for the ceiling module is likely influenced by several factors. First, the individual ribs are interconnected by the cast slab and the surrounding ring, allowing load redistribution between adjacent ribs and resulting in a more favorable structural response than that of isolated beam specimens. Furthermore, the longitudinal reinforcement differs between both structural members. While the isolated shear beams were reinforced with a single CFRP rebar, the ceiling module employed CFRP grids. The distributed arrangement of the CFRP grid enables a more uniform transfer of tensile forces into the surrounding concrete. In contrast, the concentrated cross-sectional area of a single CFRP rebar leads to a localized force transfer, which is reflected by the longitudinal cracks observed along the reinforcement in the isolated shear beams. Such cracking was not observed in the ceiling module.

Overall, the isolated shear beam tests enabled the evaluation and comparison of different CFRP shear reinforcement concepts under well-defined boundary conditions, leading to the identification of the most suitable reinforcement configuration. The large-scale ceiling module further demonstrated that, although the governing failure mechanism remained unchanged, additional structural effects enhanced the overall load-bearing capacity.

9.6 Case study

To demonstrate the practical application of the investigated ceiling module, a case study of a multi-story residential building is carried out. A point-supported slab system is designed to accommodate typical residential loads as specified in [70]. The slab is subjected to a self-weight of 2.0 kN/m^2 and a live load of 2.0 kN/m^2, representing standard loading conditions. This results in a total design load of 5.7 kN/m^2, in accordance with [71]. For a span of 4.5 m, the resulting design load on the column is $F_{\mathrm{Ed}} = 115$ kN. The design resistance is derived from the experimental failure load of 283.3 kN by applying a safety factor of $\gamma_c = 1.5$ and a β-coefficient of 1.1 for internal columns according to [41]. This results in a design resistance of 172 kN. Consequently, the design resistance exceeds the applied load by a factor of approximately 1.5, demonstrating that the investigated system is capable of fulfilling structural requirements.

10 Conclusion

This study demonstrates that multimodal digital fabrication combining extrusion-based 3DCP, casting, and integrated CFRP reinforcement enables the production of structurally efficient reinforced concrete members with highly adaptable geometries. The proposed fabrication strategy allows reinforcement integration directly within the layer-wise manufacturing process and thereby establishes a close connection between fabrication technology, structural detailing, and load-adapted design.

Overall, the proposed multimodal fabrication process proved well applicable to the investigated geometries and enabled the coordinated integration of printing, casting, and reinforcement. For increasingly complex and material-efficient geometries, particular attention should be given to geometric accuracy, reinforcement integration, and the coordination of printing and casting. Furthermore, appropriate reinforcement detailing and anchorage strategies are essential

to ensure shear integrity and effective load transfer in slender load-adapted members.

The experimental investigations showed that the structural performance of digitally fabricated concrete members is governed not only by the material properties of the concrete itself, but predominantly by fabrication-induced interaction mechanisms such as interlayer bonding, anisotropic load transfer, and reinforcement anchorage. In particular, the bond behavior between reinforcement and 3DCP was found to strongly depend on local deposition conditions and reinforcement layout. Increasing nozzle inclination improved concrete consolidation around the reinforcement and significantly enhanced bond capacity, while insufficient concrete penetration between adjacent reinforcement strands reduced the effective anchorage performance. Furthermore, thermoformed hook-shaped reinforcement ends considerably increased anchorage resistance and enabled a more effective activation of the reinforcement.

The flexural investigations demonstrated that established sectional analysis approaches can successfully predict the bending behavior of digitally fabricated CFRP-reinforced concrete members when appropriate material properties are considered. The experimentally observed flexural resistance of the investigated T-beam was reproduced with high accuracy, indicating that the global bending response of multimodally fabricated members can be assessed using mechanics-based reinforced concrete design methods.

In contrast, the shear investigations revealed that existing guideline-based design approaches developed for conventionally cast concrete significantly overestimate the concrete contribution to the shear resistance of 3DCP members. The experiments clearly showed that the layer-wise fabrication process and the resulting anisotropic material behavior fundamentally modify crack propagation, shear transfer mechanisms, and the activation of shear reinforcement. Compared to the cast reference specimen, the 3D-printed beams exhibited lower shear capacities, indicating an influence of interlayer interfaces and bond conditions. However, this comparison should be interpreted qualitatively, as the cast reference specimen originated from a separate test series and differed in its longitudinal reinforcement ratio.

To address these effects, the *Shear Crack Propagation Theory* (SCPT) was extended by explicitly incorporating interface delamination along printed layer boundaries. The proposed framework enables a mechanics-based representation of crack propagation and interface degradation in 3DCP members. In combination with experimentally derived bond-based reinforcement contributions, the developed hybrid approach reproduced the experimentally observed shear capacities with deviations below 9%, indicating that the governing mechanisms of shear failure in reinforced 3DCP members can be captured with satisfactory accuracy.

Overall, the results demonstrate that the structural design of digitally fabricated concrete members cannot rely solely on empirical adaptations of existing reinforced concrete design equations. Instead, reliable and material-efficient design approaches for 3D-printed reinforced concrete require mechanics-based models that explicitly account for fabrication-induced anisotropy, interface behavior, crack propagation, and reinforcement activation. The presented multimodal fabrication strategy, together with the proposed modeling approaches therefore enables an important step toward structurally optimized, automated, and code-compliant concrete construction by means of digital fabrication technologies.

Nevertheless, the presented reinforcement concept was developed for the proposed multimodal fabrication process and should be further validated for alternative reinforcement configurations, structural geometries as well as loading scenarios. Likewise, the applicability of the proposed SCPT framework should be verified using suitable bond stress-slip laws as well as additional experimental data covering different reinforcement concepts, manufacturing processes as well as material characteristics. Finally, future research should focus on the automated integration and positioning of preformed reinforcement to further increase the level of process automation and facilitate industrial implementation.

Acknowledgements This work was funded by the Deutsche Forschungsgemeinschaft (DFG, German Research Foundation) under the Priority Program SPP 2187: Adaptive modularized constructions made in flux under Grant (510048037) and the Germany's Excellence Strategy–EXC 3115: CARE–Climate-Neutral And Resource-Efficient Construction under Grant (533767731). The authors gratefully acknowledge the industry

partners Saint-Gobain Weber and solidian GmbH for material support.

Author contributions Engel Sven: Writing—original draft, Visualization, Project administration, Methodology, Investigation, Conceptualization. Dilkin Eduarda: Writing—original draft, Investigation. Classen Martin: Writing—review & editing, Methodology, Funding acquisition, Conceptualization.

Funding Open Access funding enabled and organized by Projekt DEAL. Deutsche Forschungsgemeinschaft, 510048037, Martin Classen, 533767731, Martin Classen.

Data availability Data will be made available on request.

Declarations

Conflict of interest The authors declare the following financial interests/personal relationships which may be considered as potential conflict of interest: Martin Classen reports financial support was provided by German Research Foundation. If there are other authors, they declare that they have no known conflict of financial interests or personal relationships that could have appeared to influence the work reported in this paper.

Open Access This article is licensed under a Creative Commons Attribution 4.0 International License, which permits use, sharing, adaptation, distribution and reproduction in any medium or format, as long as you give appropriate credit to the original author(s) and the source, provide a link to the Creative Commons licence, and indicate if changes were made. The images or other third party material in this article are included in the article's Creative Commons licence, unless indicated otherwise in a credit line to the material. If material is not included in the article's Creative Commons licence and your intended use is not permitted by statutory regulation or exceeds the permitted use, you will need to obtain permission directly from the copyright holder. To view a copy of this licence, visit http://creativecommons.org/licenses/by/4.0/.

References

1. IEA (2018) 2018 Global status report (English and other languages)—analysis - *IEA* [online]. https://www.iea.org/reports/2018-global-status-report [Zugriff am: 9 Jul 2025]
2. Cheng D et al (2023) Projecting future carbon emissions from cement production in developing countries. Nat Commun 14(1):8213. https://doi.org/10.1038/s41467-023-43660-x
3. Rettinger M et al (2025) Design for manufacturing and assembly als Entwurfsprinzip für den modularen Betonfertigteilbau. Bautechnik 102(8):458–470. https://doi.org/10.1002/bate.70001
4. Neef T et al (2025) Automated fabrication of single-curved carbon textile-reinforced concrete shells using extrusion-based printing. Dev Built Environ 23:100721. https://doi.org/10.1016/j.dibe.2025.100721
5. Engel S, Hegger J, Classen M (2024) Automated manufacturing process and structural performance of ribbed CRC slabs. 4th RILEM international conference on concrete and digital fabrication. Munich. Springer, https://doi.org/10.24355/dbbs.084-202408200559-0
6. Ramakrishnan S et al (2021) Concrete 3D printing of lightweight elements using hollow-core extrusion of filaments. Cem Concr Compos 123:104220. https://doi.org/10.1016/j.cemconcomp.2021.104220
7. Khajavi SH et al (2021) Additive manufacturing in the construction industry: the comparative competitiveness of 3D concrete printing. Appl Sci 11(9):3865. https://doi.org/10.3390/app11093865
8. (2026) Large-scale 3D printing by a team of mobile robots [online]. https://www.sciencedirect.com/science/article/pii/S0926580518304011 [Zugriff am: 13 Mai 2026]
9. Engel S et al (2026) Flow production of a modular, material-efficient CFRP-reinforced concrete ceiling system using multimodal robotic fabrication. Beton- und Stahlbetonbau. https://doi.org/10.1002/best.70154
10. Ivaniuk E et al (2024) Automated manufacturing of reinforced modules of segmented shells based on 3D printing with strain-hardening cementitious composites. Autom Constr 166:105591. https://doi.org/10.1016/j.autcon.2024.105591
11. Lim JH, Weng Y, Pham Q-C (2020) 3D printing of curved concrete surfaces using adaptable membrane formwork. Constr Build Mater 232:117075. https://doi.org/10.1016/j.conbuildmat.2019.117075
12. Vasilic K (2024) Standardization aspects of concrete 3D printing. RILEM Tech Lett 9:98–105. https://doi.org/10.21809/rilemtechlett.2024.201
13. Asprone D et al (2018) Rethinking reinforcement for digital fabrication with concrete. Cement Concr Res 112:111–121. https://doi.org/10.1016/j.cemconres.2018.05.020
14. Engel S, Hegger J, Classen M (2025) Multimodal automated fabrication with concrete: case study and structural performance of ribbed CFRP-reinforced concrete ceilings. Addit Manuf 101:104689. https://doi.org/10.1016/j.addma.2025.104689
15. Meurer M, Classen M (2021) Mechanical properties of hardened 3D printed concretes and mortars-development of a consistent experimental characterization strategy. Materials 14(4):752. https://doi.org/10.3390/ma14040752
16. Weng Y et al (2021) Synchronized concrete and bonding agent deposition system for interlayer bond strength enhancement in 3D concrete printing. Autom Constr 123:103546. https://doi.org/10.1016/j.autcon.2020.103546
17. Schmidt C, Hegger J (2025) Experimental investigations on bond behaviour and crack development in concrete members reinforced with carbon textile grids subjected to cyclic loading. Constr Build Mater 466:140168. https://doi.org/10.1016/j.conbuildmat.2025.140168
18. Classen M (2020) Shear crack propagation theory (SCPT)—the mechanical solution to the riddle of shear in RC members without shear reinforcement. Eng Struct. https://doi.org/10.1016/j.engstruct.2020.110207
19. Sinning A, Claßen M, Hegger J (2025) Zum Einfluss von druckmembrankräften auf die querkrafttragfähigkeit von plattenstreifen ohne querkraftbewehrung/On

the influence of compressive membrane forces on shear capacity of slab segments without shear reinforcement. Bauingenieur 100(09):249–259. https://doi.org/10.37544/0005-6650-2025-09-45
20. Dilkin E et al (2026) Shear behaviour of 3D-printed carbon-reinforced concrete beams: an extension of a physics-based crack propagation model (in preparation)—proceedings of the FIB congress 2026, Lisbon 2026
21. Engel S, Dilkin E, Classen M (2025) Structural performance of CFRP-reinforced concrete beams using digital fabrication techniques. Fédération internationale du béton [Ed.] 21st fib symposium. Antibes, France, pp. 2729–2737
22. Engel S, Bielak J, Classen M (2025) Rethinking concrete slabs: modular CFRP-reinforced systems for sustainable construction. Purdue University [Hrsg.] C3 symposium 2025. Chicago, USA
23. Engel S, Bielak J, Classen M (2025) Material efficient CFRP-reinforced concrete floor slabs. CICE 2025. Lisbon, Portugal
24. Bos FP, Bosco E, Salet TAM (2019) Ductility of 3D printed concrete reinforced with short straight steel fibers. Virt Phys Prototyp 14(2):160–174. https://doi.org/10.1080/17452759.2018.1548069
25. Yang Y et al (2022) 3D-printing ultra-high performance fiber-reinforced concrete under triaxial confining loads. Addit Manuf 50:102568. https://doi.org/10.1016/j.addma.2021.102568
26. Bos FP et al (2017) Experimental exploration of metal cable as reinforcement in 3D printed concrete. Materials (Basel). https://doi.org/10.3390/ma10111314
27. Mechtcherine V et al (2020) Extrusion-based additive manufacturing with carbon reinforced concrete: concept and feasibility study. Materials (Basel). https://doi.org/10.3390/ma13112568
28. (2026) 3D printing of mortar with continuous fibres: principle, properties and potential for application [online]. https://www.sciencedirect.com/science/article/pii/S0926580521002570 [Zugriff am: 13 Mai 2026]
29. Caron J-F et al (2021) 3D printing of mortar with continuous fibres: principle, properties and potential for application. Autom Constr 129:103806. https://doi.org/10.1016/j.autcon.2021.103806
30. Gebhard L et al (2022) Inter-laboratory study on the influence of 3D concrete printing set-ups on the bond behaviour of various reinforcements. Cem Concr Compos 133:104660. https://doi.org/10.1016/j.cemconcomp.2022.104660
31. Scott C (2016) Chinese construction company 3D prints an entire two-story house on-site in 45 days [online]. https://3dprint.com/138664/huashang-tengda-3d-print-house/ [Zugriff am: 11 Dez 2021]
32. Marchment T, Sanjayan J (2020) Mesh reinforcing method for 3D concrete printing. Autom Constr. https://doi.org/10.1016/j.autcon.2019.102992
33. Zhang S et al (2024) Prototypical realization of fully automated 3D-printing of reinforced concrete using AMoRC method. Digital concrete. Universitätsbibliothek Braunschweig, München, Deutschland
34. Zhang S et al (2023) Development of an innovative 3D-printing process for reinforced concrete—AMoRC method. In: Jędrzejewska A et al [Hrsg.] SynerCrete23. Milos Island, Greece. Cham: Springer Nature Switzerland, 641–652
35. Claßen M, Claßen J, Sharma R (2020) Konzeptionierung eines praxisorientierten 3D-Druckverfahrens für den Verbundwerkstoff Stahlbeton (AMoRC). Beton Stahlbetonbau 115(12):934–942. https://doi.org/10.1002/best.202000023
36. Hass L, Bos F (2020) Bending and pull-out tests on a novel screw type reinforcement for extrusion-based 3D printed concrete. In: Bos FP et al [Hrsg.] Second RILEM international conference on concrete and digital fabrication. Cham: Springer International Publishing, S. 632–645
37. Mechtcherine V et al. Concrete printing with textile reinforcement: approaches, classification, and testing. Cem Concr Res. https://doi.org/10.1016/j.cemconres.2026.108340
38. Baktheer A, Classen M (2024) A review of recent trends and challenges in numerical modeling of the anisotropic behavior of hardened 3D printed concrete. Addit Manuf 89:104309. https://doi.org/10.1016/j.addma.2024.104309
39. ter Haar B, Kruger J, van Zijl G (2024) Off-site 3D printed concrete beam design and fabrication. J Build Eng 89:109117. https://doi.org/10.1016/j.jobe.2024.109117
40. Zhang S et al (2026) Integrating arc stud welding and spatial steel reinforcement into 3D concrete printing for robotic fabrication of reinforced concrete structures. Autom Constr. https://doi.org/10.1016/j.autcon.2026.107113
41. DIN EN 1992-1-1:2025-09 (2025) Eurocode 2: bemessung und konstruktion von stahlbeton- und spannbetontragwerken-Teil 1-1: allgemeine regeln und regeln für hochbauten, Brücken und ingenieurbauwerke —deutsche fassung EN 1992-1-1:2023. Berlin
42. Hu X, Shahzad Q, Li F (2025) Influence of the shear span ratio on the shear performance of 3D-printed concrete beams without web reinforcement. Structures 76:109023. https://doi.org/10.1016/j.istruc.2025.109023
43. Engel S et al (2026) Multimodaler robotischer Fließfertigungsprozess—automatisierte herstellung eines modularen, materialeffizienten CFK-bewehrten betondeckensystems. Beton Stahlbetonbau. https://doi.org/10.1002/best.70179
44. Deutscher Ausschuss für Stahlbeton (2024) Erläuterungen und beispiele zur dafstb-richtlinie betonbauteile mit nichtmetallischer bewehrung—DAfStb-Heft 660. DIN Media
45. Spelter A (2023) Long-term durability of carbon reinforced concrete [Dissertation]. RWTH Aachen University. https://publications.rwth-aachen.de/record/960708
46. Spelter A et al (2019) Long-term durability of carbon-reinforced concrete: an overview and experimental investigations. Appl Sci. https://doi.org/10.3390/app9081651
47. Solidian GmbH (2026) solidian ANTICRACK Q95-CCE-38 Technical product data sheet v2406
48. Bielak J (2021) Shear in slabs with non-metallic reinforcement [Dissertation]. RWTH Aachen University
49. Saint Gobain Weber (2024) 3D printing materials - Specifics - Weber 3D 160-1 [online]. www.3d.weber/en/3d-printing-service/3d-printing-materials [Zugriff am: 27 Nov 2024]

50. Bos F et al (2025) Mechanical properties of 3D printed concrete: a RILEM TC 304-ADC interlaboratory study—approach and main results. Mater Struct 58(5):183. https://doi.org/10.1617/s11527-025-02686-x
51. Wolfs R et al (2025) Mechanical properties of 3D printed concrete: a RILEM TC 304-ADC interlaboratory study—flexural and tensile strength [online]. Springer. https://link.springer.com/article/https://doi.org/10.1617/s11527-025-02687-w [Zugriff am: 11 Mai 2026]
52. Mechtcherine V et al (2025) Mechanical properties of 3D printed concrete: a RILEM 304-ADC interlaboratory study—compressive strength and modulus of elasticity. Mater Struct 58(5):181. https://doi.org/10.1617/s11527-025-02688-9
53. Schmidt C, Classen M, Hegger J (2024) Bond behaviour and crack width prediction in non-metallic textile-reinforced concrete members. In: Mechtcherine V, Signorini C, Junger D [Hrsg.] Transforming construction: advances in fiber reinforced concrete: XI RILEM-fib international symposium on fiber reinforced concrete (BEFIB 2024). Cham: Springer Nature Switzerland, S. 642–651
54. DIN EN 196-1:2016-11 (2016) Prüfverfahren für zement-teil 1: bestimmung der festigkeit–deutsche fassung EN 196-1:2016. Berlin: Beuth
55. DIN EN 12390-13:2021-09 (2021) Prüfung von Festbeton–Teil 13: bestimmung des elastizitätsmoduls unter druckbelastung (Sekantenmodul)–Deutsche Fassung EN 12390-13:2021. Berlin: Beuth
56. solidian, kelteks (2026) Bewehrungsstäbe: REBAR carbon [online]. https://www.solidian-kelteks.com/de/produkte/bau/bewehrungen/bewehrungsstaebe/rebar-carbon-detail [Zugriff am: 12 Feb 2026]
57. Dilkin E, Classen M (2026) Shear behavior of 3D-printed concrete beams with CFRP reinforcement: an experimental parametric analysis. Preprint submitted to Engineering Structures
58. Becks H et al (2023) Monitoring the fatigue-induced strain evolution of concrete bridges using fiber optic sensors. ce/Papers 6(5):1119–1126. https://doi.org/10.1002/cepa.2033
59. Becks H et al (2025) Assessing crack formation and strain distribution in concrete structures using externally installed fiber optic sensors. Case Stud Constr Mater. https://doi.org/10.1016/j.cscm.2025.e04744
60. Becks H et al (2023) Monitoring concept for the propagation of compressive fatigue in externally prestressed concrete beams using digital image correlation and fiber optic sensors. Fatigue Fract Eng Mater Struct 46(2):514–526. https://doi.org/10.1111/ffe.13881
61. Janiak T et al (2023) Evaluation of distributed fibre optic sensors in structural concrete. Mater Struct 56:159. https://doi.org/10.1617/s11527-023-02222-9
62. Becks H et al (2022) Application of fiber optic measurement in textile-reinforced concrete testing. Struct Concr 23(4):2600–2614. https://doi.org/10.1002/suco.202100252
63. fib bulletin 40 (2007) FRP reinforcement in RC structures–Technical report. Lausanne, Switzerland: Fédération internationale du béton (fib)
64. CNR-DT 203/2006 (2007) Guide for the design and construction of concrete structures reinforced with fiber-reinforced polymer bars
65. ACI 318-25 (2025) Building code for structural concrete—code requirements and commentary (ACI CODE-318-25)–Reported by ACI committee 318. Farmington Hills, Michigan, USA: American Concrete Institute
66. Camanho PP, Davila CG, Moura MFde (2003) Numerical simulation of mixed-mode progressive delamination in composite materials. J Compos Mater 37(16):1415–1438. https://doi.org/10.1177/0021998303034505
67. Bosbach SC (2024) Shear in carbon reinforced concrete: a physically based model to characterise the structural behaviour [Dissertation]. RWTH Aachen University
68. Engel S, Hendricks J, Classen M. Ribbed CFRP-reinforced Ceilings Reinvented: Optimization of Nervi's principles using multimodal digital fabrication methods. J Compos Constr
69. Classen M, Kalus M (2023) Punching shear response theory (PSRT)—a two degree of freedom kinematic theory for modeling the entire punching shear vs. deformation response of RC slabs and footings. Eng Struct. https://doi.org/10.1016/j.engstruct.2023.116197
70. DIN EN 1991-4:2010-12 (2010) Eurocode 1: einwirkungen auf tragwerke - teil 4: einwirkungen auf silos und flüssigkeitsbehälter–deutsche fassung EN 1991-4:2006. Berlin: Beuth Verlag GmbH
71. Firrao D (ed) (1990) Fracture behaviour and design of materials and structures—proceedings of the eighth European conference on fracture. EMAS, Warley, West Midlands

Publisher's Note Springer Nature remains neutral with regard to jurisdictional claims in published maps and institutional affiliations.